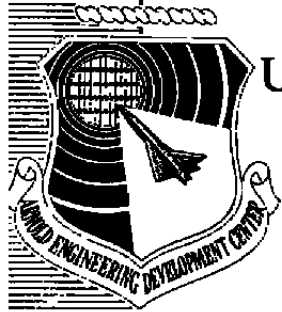$\mathcal{R}.\mathcal{C}.\mathcal{B}auer$

AEDC-TR-84-7

Unsteady Viscous-Inviscid Interaction Procedures for Transonic Airfoil Flows

T. L. Donegan
Calspan Field Services, Inc.

July 1984

Final Report for Period October 1, 1982 · September 30, 1983

ARNOLD ENGINEERING DEVELOPMENT CENTER
ARNOLD AIR FORCE STATION, TENNESSEE
AIR FORCE SYSTEMS COMMAND
UNITED STATES AIR FORCE

NOTICES

When U. S. Government drawings, specifications, or other data are used for any purpose other than a definitely related Government procurement operation, the Government thereby incurs no responsibility nor any obligation whatsoever, and the fact that the government may have formulated, furnished, or in any way supplied the said drawings, specifications, or other data, is not to be regarded by implication or otherwise, or in any manner licensing the holder or any other person or corporation, or conveying any rights or permission to manufacture, use, or sell any patented invention that may in any way be related thereto.

Qualified users may obtain copies of this report from the Defense Technical Information Center.

References to named commercial products in this report are not to be considered in any sense as an endorsement of the product by the United States Air Force or the Government.
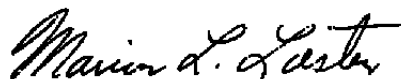
APPROVAL STATEMENT

This report has been reviewed and approved.

KEITH L. KUSHMAN
Directorate of Technology
Deputy for Operations

Approved for publication:

FOR THE COMMANDER

MARION L. LASTER
Director of Technology
Deputy for Operations

REPORT DOCUMENTATION PAGE

1a REPORT SECURITY CLASSIFICATION UNCLASSIFIED		1b. RESTRICTIVE MARKINGS			
2a. SECURITY CLASSIFICATION AUTHORITY		3 DISTRIBUTION/AVAILABILITY OF REPORT Approved for public release; distribution unlimited.			
2b. DECLASSIFICATION/DOWNGRADING SCHEDULE					
4 PERFORMING ORGANIZATION REPORT NUMBER(S) AEDC-TR-84-7		5 MONITORING ORGANIZATION REPORT NUMBER(S)			
6a. NAME OF PERFORMING ORGANIZATION Arnold Engineering Development Center	6b. OFFICE SYMBOL (If applicable) DOF	7a. NAME OF MONITORING ORGANIZATION			
6c. ADDRESS (City, State and ZIP Code) Air Force Systems Command Arnold Air Force Station, TN 37389		7b. ADDRESS (City, State and ZIP Code)			
8a. NAME OF FUNDING/SPONSORING ORGANIZATION Arnold Engineer- ing Development Center	8b. OFFICE SYMBOL (If applicable) DO	9. PROCUREMENT INSTRUMENT IDENTIFICATION NUMBER			
8c ADDRESS (City, State and ZIP Code) Air Force Systems Command Arnold Air Force Station, TN 37389		10 SOURCE OF FUNDING NOS.			

		PROGRAM ELEMENT NO	PROJECT NO.	TASK NO.	WORK UNIT NO
		65807F			

11 TITLE (Include Security Classification) See Reverse of This Page			

12. PERSONAL AUTHOR(S)
Donegan, T.L., Calspan Field Services, Inc., AEDC Division

13a. TYPE OF REPORT Final	13b. TIME COVERED FROM 10/1/82 TO 9/30/83	14 DATE OF REPORT (Yr., Mo., Day) July 1984	15. PAGE COUNT 57

16. SUPPLEMENTARY NOTATION

Available in Defense Technical Information Center (DTIC).

17.	COSATI CODES		18 SUBJECT TERMS (Continue on reverse if necessary and identify by block number)
FIELD	GROUP	SUB GR.	aerodynamic characteristics flow
20	04		Navier-Stokes equations boundary layer
14	02		interactions transonic flow

19. ABSTRACT (Continue on reverse if necessary and identify by block number)

    This study is concerned with the development of a computational algorithm for viscous-inviscid interactions with application to two-dimensional transonic airfoil flows. The inner viscous flow is computed by the integral method of Whitfield, while the external flow is calculated by Jameson's Euler equation code. The two flows are matched by a linearized boundary condition at the airfoil surface. Of particular interest is the use of a time-dependent boundary-layer calculation method since it has been determined that a time-dependent method is desirable for extending the interaction method to three-dimensional flows. In general, it is found that the agreement between theoretical prediction and experimental data is satisfactory for engineering calculations.

20 DISTRIBUTION/AVAILABILITY OF ABSTRACT UNCLASSIFIED/UNLIMITED ☐ SAME AS RPT. ☒ DTIC USERS ☐	21 ABSTRACT SECURITY CLASSIFICATION UNCLASSIFIED	
22a. NAME OF RESPONSIBLE INDIVIDUAL W.O. Cole	22b TELEPHONE NUMBER (Include Area Code) (615) 455-2611/Ext.7813	22c OFFICE SYMBOL DOS

DD FORM 1473, 83 APR   EDITION OF 1 JAN 73 IS OBSOLETE

TITLE.

Unsteady Viscous-Inviscid Interaction Procedures for Transonic Airfoil Flows

PREFACE

CONTENTS

ILLUSTRATIONS

Figure

1.0 INTRODUCTION

Analysis of aerodynamic flows is used to support the development and evaluation of weapons systems tested in the ground test facilities at AEDC. Aerodynamic solutions are used in experimental test planning, test execution, and post-test analysis to increase test facility productivity, upgrade test data quality, and reduce test expense. The most direct approach to the computation of turbulent viscous flows, which are the types of flows usually encountered at AEDC, is to solve the Reynolds-averaged Navier-Stokes equations. Critical flow areas such as separated flows and shock/boundary layer interactions may be computed in this manner, thereby aiding in the evaluation of a specific test article or facility.

Algorithms for solving the Navier-Stokes equations are extremely complex and require extensive computer resources. Therefore, it is economically expedient to explore alternative solution techniques which may be used in a flow evaluation without large computer resource requirements. An inexpensive approach to the problem is by means of a component method based on the assumption that the boundary-layer equations adequately describe the viscous layer near a wall or model, and that the exterior flow may be described by the inviscid equations. These two regions of flow may then be matched at a common boundary, usually the boundary-layer edge.

This component type of flow solver has been shown to be an effective tool in the computation of viscous-inviscid interacting flows as cited by Lock (Ref. 1), Melnik (Ref. 2), and Le Balleur (Ref. 3). This method was demonstrated for two-dimensional and axisymmetric bodies with small separated flow regions in Ref. 4. Analysis of separated flows may be accomplished by computing the boundary-layer equations using an inverse method. A review of computational methods capable of separated flow solutions is given by Le Balleur (Ref. 3). An extension of inverse component methods to three-dimensional problems is feasible and has the potential for computing separated viscous flows over complex bodies with significantly less computer resources than Navier-Stokes methods.

The component method may be referred to as the viscous-inviscid interaction procedure. Calculation of the inviscid exterior flow field can be obtained by solution of the Euler equations which approximate the Navier-Stokes equations as the Reynolds number approaches infinity (and removes all energy dissipation processes from the flow). The interior region may be computed with the boundary-layer equations obtained by imposing the Prandtl limit to the Navier-Stokes equations and may be approximately solved by the integral method. The exterior and interior regions about an airfoil are depicted in Fig. 1.

A steady interaction code[1] (one in which the boundary-layer solution method is not time-dependent) exists. It employs a two-dimensional integral compressible boundary-layer

---

[1] The terms "steady" and "unsteady" interactions refer to the boundary layer portion of the code only. The Euler code is time-dependent for both cases.
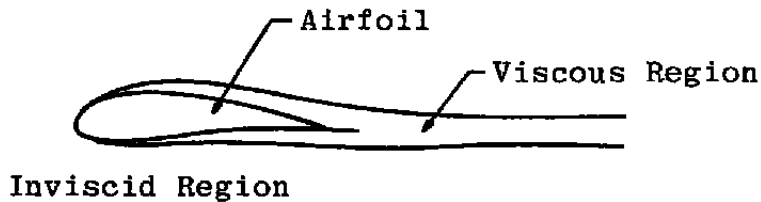
Figure 1. Flow regions about an airfoil.

method, developed by Whitfield (Ref. 5), in conjunction with a three-dimensional, time-dependent Euler code (Ref. 6). The two-dimensional boundary-layer method can be applied to a three-dimensional wing by using strip theory when the crossflow is small (since boundary layers are sensitive to small crossflow pressure gradients). Calculations of two-dimensional boundary layers are made at various spanwise cross sections. However, there exists a need for a fully three-dimensional viscous interaction method to be used for finite wing applications. This would allow flows to be analyzed with the boundary layers computed over complete wings.

There are problems associated with a three-dimensional viscous-inviscid interaction code. In two-dimensional boundary-layer codes, the solution process marches in the flow direction and computes boundary-layer quantities at each spatial station. In three-dimensional problems the solution process is restricted to one direction but there are two computational directions (e.g., the chordwise and spanwise directions on a finite wing). If this problem is alleviated by aligning the computational mesh on the body with the flow direction, the mesh becomes flow-dependent and must be altered after each update to the flow. This makes any solution process both difficult and lengthy because of the constant altering of the mesh between the inviscid code and the boundary-layer code. Therefore, it would be useful to produce a boundary-layer method which utilizes the spacing of the inviscid mesh and still provides a solution on a three-dimensional body. This can be accomplished if the boundary-layer equations include the time-dependent terms and the entire boundary-layer on the body is solved at each instant in time. The solution process could march by means of a time-stepping parameter until a steady-state solution is obtained.

However, before three-dimensional flow solutions are attempted by the unsteady boundary-layer method, attention should be focused on simpler two-dimensional problems solved by the same method. This allows exploration of the characteristics of the unsteady formulation without the complications associated with another added dimension. The unsteady results can be validated by comparisons with solutions obtained from the two-dimensional steady interaction code.

The intention of this work is to produce the unsteady interaction code and compare its solution with that of the steady interaction code and with data.

2.0. DERIVATION OF THE UNSTEADY INTEGRAL BOUNDARY-LAYER EQUATIONS FOR TWO-DIMENSIONAL COMPRESSIBLE FLOW

The inner region solution is constructed from the integral form of the boundary-layer equations. These equations are obtained via the Reynolds-averaged Navier-Stokes equations and the Prandtl limit. Thus, when expressed in conservation form, the Navier-Stokes equations are (Ref. 7):

$$\frac{\partial G}{\partial t} + \frac{\partial}{\partial x_j} F_{ij} = 0, \tag{1}$$

where

$$G = \begin{pmatrix} \varrho \\ \varrho v_i \\ e \end{pmatrix} \tag{2}$$

and

$$F_{ij} = \begin{pmatrix} 0 \\ -\tau_{ij} \\ -\tau_{kj} v_k + q_j \end{pmatrix} + G v_j \equiv f_{ij}(\mu) + G v_j \tag{3}$$

are the dependent variable matrices and

$$\tau_{ij} = \mu \left(\frac{\partial v_i}{\partial x_j} + \frac{\partial v_j}{\partial x_i} \right) - p\delta_{ij} + \lambda \frac{\partial v_k}{\partial x_k} \delta_{ij} \tag{4}$$

is the viscous stress tensor expressed in terms of the Lamé constants μ and λ (usually referred to as the first and second coefficients of viscosity, respectively) and δ_{ij} is the Kronecker delta. These constants are related to the bulk coefficient of viscosity, η, by the equality, $\eta = \lambda + 2\mu/3$, and this quantity is placed equal to zero by adopting Stokes' hypothesis. The equation of state is taken to be

$$e = \frac{p}{\gamma\text{-}1} + \frac{1}{2} \varrho v_i v_i \tag{5}$$

Finally, $q_i = -k\partial T/\partial x_i$ is the heat flux component in the x_i direction and k is the thermal conductivity. The form of Eq. (1) remains intact under the Euler limit operator (E such that $\mu \to 0, \lambda \to 0, k \to 0$), but

7

$$E(f_{ij}) \rightarrow \begin{pmatrix} 0 \\ p\delta_{ij} \\ pv_j \end{pmatrix} \qquad (6)$$

is the limit form of f_{ij}, and all dissipation-causing terms vanish.

Before the Euler limit operator is applied to Eq. (1) it is necessary to introduce the Reynolds decomposition in the form:

$$\phi = \Phi + \psi', \qquad (7)$$

where

$$\Phi = \tilde{E}\ (\phi) \text{ and } \tilde{E}\ (\psi') = 0, \qquad (8)$$

with $\tilde{E}$ an averaging operator. The Reynolds-averaged equations then follow when the operator $\tilde{E}$ is applied to the decomposed equations. All nonlinear terms give rise to correlations of variable fluctuations. For example, a velocity product — which arises in the inertia term of the momentum equation — will produce $<\varrho v_i' v_j'>$ correlations whose dimensional form allows them to be referred to as Reynolds stresses.

The Euler equations are recovered (as the appropriate outer flow equations) when the Euler limit operator E is applied to the Reynolds-averaged equations if it can be assumed that all correlation terms vanish in the far field. This need not be true for all flows of interest: examples to the contrary include wind tunnel flows and atmospheric flows. It is well known that free-stream turbulence can have a significant effect on the development of a turbulent boundary layer and this fact may well impair the comparison between wind tunnel data and theoretical calculations based upon the classical Euler equations for the external flow. Nevertheless, the present study neglects the correlation terms in the Euler limit equations.

The inner region equations are obtained from the Reynolds-averaged equations by use of the Prandtl limit operator P, where P is a product operator such that:

1. The coordinate (x_2, say) normal to the wall is scaled as $\xi = x_2/\sqrt{\nu}$ for laminar flows. Such scaling is usually adopted for turbulent flow without justification.

2. The operator E is applied.

The result of this combined operation is the pair of equations (now expressed in planar coordinates, where u and v are the velocity components in the x- and y-directions, respectively):

8

$$\frac{\partial \varrho}{\partial t} + \frac{\partial}{\partial x}(\varrho u) + \frac{\partial}{\partial y}(\varrho v) = 0 \tag{9}$$

$$\varrho \frac{\partial u}{\partial t} + \varrho u \frac{\partial u}{\partial x} + \varrho v \frac{\partial u}{\partial y} = -\frac{dp}{dx} + \frac{\partial \tau}{\partial y}, \tag{10}$$

in which

$$\tau = \mu \frac{\partial u}{\partial y} - <\varrho u'v'> \tag{11}$$

represents the total shear stress component which has the major impact on a two-dimensional boundary layer.

These partial differential equations may be transformed into ordinary differential equations in space by multiplying Eq. (9) by $u^{m+1}/(m+1)$, and Eq. (10) by u^m, and summing the two equations to form the mth-moment equation:

$$\frac{1}{m+1}\left\{ \frac{\partial}{\partial t}\left(\varrho u^{m+1} - \varrho u_e^{m+1}\right) + \frac{\partial}{\partial x}\left[\varrho_e u_e^{m+2}\left(\frac{\varrho u}{\varrho_e u_e}\frac{u^{m+1}}{u_e^{m+1}} - 1\right)\right] + \frac{\partial}{\partial y}\left(\varrho v u^{m+1}\right) \right.$$
$$\left. - u_e^{m+1}\frac{\partial}{\partial y}(\varrho v)\right\} + \varrho u_e^m \frac{\partial u_e}{\partial t} + \varrho u u_e^m \frac{\partial u_e}{\partial x} = u^m \varrho_e \frac{\partial u_e}{\partial t}$$
$$+ u^m \varrho_e u_e \frac{\partial u_e}{\partial x} + u^m \frac{\partial \tau}{\partial y} \tag{12}$$

where $m = 0$ generates the momentum equation, and $m = 1$ creates the mean flow kinetic energy equation. The momentum equation valid at the edge of the boundary layer has been incorporated to replace the pressure gradient, dp/dx, but does not imply the assumption of isentropic flow.

The integral momentum equation is obtained by integrating Eq. (12) from $0 \le y < \infty$, setting $m = 0$ and introducing the integral parameters

$$\delta^* = \int_o^\infty \left(1 - \frac{\varrho u}{\varrho_e u_e}\right) dy, \tag{13}$$

$$\theta = \int_o^\infty \frac{\varrho u}{\varrho_e u_e}\left(1 - \frac{u}{u_e}\right) dy, \tag{14}$$

9

$$\theta_\varrho = \int_0^\infty \left(1 - \frac{\varrho}{\varrho_e} \right) dy, \tag{15}$$

$$c_f = \frac{\tau_0}{\frac{1}{2} \varrho_e u_e^2}, \tag{16}$$

in which δ^* is the displacement thickness whose significance will be discussed in Section 5.0; θ is the momentum thickness or the distance that the momentum defect extends from the body; θ_ϱ is the density thickness; and c_f is the local skin friction coefficient with $\tau_0 = \mu \partial u / \partial y|_{y=0}$ since the Reynolds stress vanishes on the wall. Then by applying the boundary conditions

$$u = 0; \; v = 0 \text{ at } y = 0$$

$$u \to u_e; \; \tau \to 0 \text{ as } y \to \infty$$

the integral momentum equation becomes

$$\frac{1}{\varrho_e u_e^2} \underbrace{\left[\frac{\partial}{\partial t} (\varrho_e u_e \delta^*) - u_e \frac{\partial}{\partial t} (\varrho_e \theta_\varrho) \right]}_{\text{\textcircled{A}}} + \underbrace{\frac{1}{\varrho_e u_e^2} \frac{\partial}{\partial x} (\varrho_e u_e^2 \theta)}_{\text{\textcircled{B}}}$$

$$+ \underbrace{\frac{\delta^*}{u_e} \frac{\partial u_e}{\partial x}}_{\text{\textcircled{C}}} - \underbrace{\frac{c_f}{2}}_{\text{\textcircled{D}}} = 0 \tag{17}$$

The source term $\text{\textcircled{A}}$ derives from the time-dependent terms in Eqs. (9) and (10) and has two components involving δ^* and θ_ϱ which come from both the continuity and momentum equations. Term B describes the rate of change of momentum thickness θ as the boundary layer develops under the imposed pressure gradient. The pressure gradient is contained in term $\text{\textcircled{C}}$ (here expressed as an external velocity gradient where, as pointed out above, the flow has not been assumed to be isentropic). Term $\text{\textcircled{C}}$ thus represents the external flow boundary condition. Finally, term $\text{\textcircled{D}}$ represents the only contribution of the shear stress τ to the momentum integral equation and contains only the boundary value $\tau_0 = \mu \partial u / \partial y|_{y=0}$. The skin friction coefficient c_f is included empirically and is usually expressed in the form $c_f = c_f(R_e\theta, H, M)$, as discussed in Section 3.0.

The mean flow kinetic energy equation is obtained by setting m = 1 in Eq. (12), integrating from $0 \le y < \infty$ and introducing the integral parameters

$$\delta_u^* = \int_0^\infty \left(1 - \frac{u}{u_e}\right) dy, \tag{18}$$

$$\theta^* = \int_0^\infty \frac{\varrho u}{\varrho_e u_e} \left(1 - \frac{u^2}{u_e^2}\right) dy, \tag{19}$$

$$D_E = \int_0^\infty \frac{\tau}{\tau_0} \frac{\partial}{\partial y}\left(\frac{u}{u_e}\right) dy, \tag{20}$$

in which δ_u^* is the velocity thickness; θ^* is the energy dissipation thickness; and D_E is the shear work integral term. Then by applying the previous boundary conditions, the mean flow kinetic energy equation (or first moment equation) becomes

$$\frac{1}{2\varrho_e u_e^3} \frac{\partial}{\partial t} \varrho_e u_e^2 (\theta + \delta^* - \theta_\varrho) + \underbrace{\frac{\theta_\varrho - \delta_u^*}{u_e^2} \frac{\partial u_e}{\partial t}}_{\text{(A)}} + \underbrace{\frac{1}{2\varrho_e u_e^3} \frac{\partial}{\partial x}(\varrho_e u_e^3 \theta^*)}_{\text{(B)}}$$

$$+ \underbrace{\frac{\delta^* - \delta_u^*}{u_e} \frac{\partial u_e}{\partial x}}_{\text{(C)}} - \underbrace{\frac{c_f D_E}{2}}_{\text{(D)}} = 0 \tag{21}$$

Term (A) is again a source term and term (C) involves the external pressure gradient. Term (B) is the rate of change of mean flow kinetic energy thickness θ^*. Term (D), containing the shear work integral D_E, is the most interesting term since this is the major contribution from the Reynolds shear stress $<\varrho u'v'>$. From Eq. (20) it is seen that the shear work integral involves an integral of the quantity $\tau \partial u/\partial y$ across the boundary layer.

If Eqs. (17) and (21) are formed for the three-dimensional problem, several differences would be evident. Two momentum equations, each with three velocity terms, would be required in addition to the three-dimensional unsteady continuity equation. Also, a second shear stress term would be required for the spanwise direction on a wing. Two sets of integral parameters would also be required; one in each direction of the airfoil — chordwise and spanwise.

Finally, it can be noted that Eqs. (17) and (21) contain seven unknowns $\{\delta^*, \theta, \theta^*, \theta_\varrho, \delta_u^*, c_f, D_E\}$ and can only be solved when five additional equations are available. Experimental correlations are used in this capacity in the present work, and will be discussed in Section 3.0.

3.0 STEADY AND UNSTEADY BOUNDARY-LAYER METHODS

3.1 STEADY BOUNDARY-LAYER METHODS

Many of the basic ideas used in the steady formulations are maintained in the unsteady case. A steady compressible turbulent integral boundary-layer code was developed by Whitfield, Ref. 5, to produce quick and accurate solutions to two-dimensional boundary layers on adiabatic walls. The input required is a distribution of pressure on the body which is usually obtained from experimental measurements in the present applications. (This method is referred to as the direct method. Conversely, a method using a δ^* distribution as input is termed an inverse method.) Whitfield's method solves the integral x-momentum and mean flow kinetic energy equations formulated from the differential continuity and x-momentum equations. The integral equations solved are (from Ref. 5).

$$\frac{1}{\varrho_e u_e^2} \frac{d}{dx} (\varrho_e u_e^2 \theta) + \frac{\delta^*}{u_e} \frac{du_e}{dx} = \frac{c_f}{2} \tag{22}$$

$$\frac{1}{2\varrho_e u_e^3} \frac{d}{dx} (\varrho_e u_e^3 \theta^*) + \frac{\delta^* - \delta_u^*}{u_e} \frac{du_e}{dx} = \frac{c_f}{2} D_E \tag{23}$$

These equations differ from the unsteady equations developed in Section 2.0 only by the time derivative terms [the A terms from Eqs. (17) and (21)]. The number of unknowns in Eqs. (22) and (23) is reduced to six since θ_ϱ only occurs in the unsteady terms. The correlations obtained later will be used as the remaining equations required to solve the system.

Whitfield's approach to solution of Eqs. (22) and (23) was to establish various shape factors:

$$H_{\delta^*} = \delta^*/\theta, \tag{24}$$

$$H_{\theta^*} = \theta^*/\theta, \tag{25}$$

$$H_{\delta_u^*} = \delta_u^*/\theta, \tag{26}$$

and correlate them with $\overline{H}$ and the boundary-layer edge Mach number by numerically integrating (Simpson's rule) the velocity profile of Whitfield and the expression for ϱ/ϱ_e (Ref. 5). The correlations relate compressible and incompressible flows by means of the Mach number dependence included in the correlations. In addition, the skin friction (c_f) was correlated with $\overline{H}$ and $\overline{Re}_\theta$ by using the work of Winter and Gaudet (Ref. 8), who established

12

the relationship between low-speed skin friction (c_f) and the local skin friction ($\overline{c_f}$) in a compressible flow. Their relation is

$$\frac{\overline{c_f}}{c_f} = \left(1 + \frac{M_e^2}{5}\right)^{\frac{1}{3}} \tag{27}$$

in which M_e is the Mach number at the boundary-layer edge. Initially, this relationship was established for adiabatic walls, zero pressure gradient, and air as the working fluid, but it was hypothesized (Ref. 5) that the relationship is also true if the appropriate expression for $\overline{c_f}$ is used in instances in which the pressure gradient does not vanish. A relationship for $\overline{c_f}$ was extracted from White [Ref. 9, Eq. (6.180b)] where $\overline{c_f}$ is a function of $\overline{H}$ and $\overline{Re}_\theta$; that is,

$$\overline{c_f} = 0.3\, e^{(-1.33\overline{H})}\, (\log \overline{Re}_\theta)^{(-1.74 - 0.31\overline{H})} \tag{28}$$

The correlation, Eq. (28), assumes a smooth wall. Effects of roughness could be included by introducing new parameters into the correlation.

The shear work integral term, D_E, is

$$D_E = \int_0^\infty \frac{\tau}{\tau_0} \frac{\partial}{\partial y}\left(\frac{u}{u_e}\right) dy, \tag{29}$$

which is basically a turbulent energy production term which describes the conversion of mean flow energy into turbulent energy. Equation (29) was obtained by direct integration employing the Cebeci-Smith two-layer eddy viscosity turbulence model (Ref. 10) for τ and Whitfield's turbulent velocity profile for $\partial u/\partial y$. The Cebeci-Smith turbulence model was chosen primarily because of its simplicity and computational speed. However, the shear work integral term was later numerically correlated with $\overline{H}$, edge Mach number, M_e, and $\overline{Re}_\theta$ as reported in Ref. 11. As a result, all terms in the steady integral equations [Eqs. (22) and (23)] are either input, or may be determined by the correlations. The integral equations are then solved by the predictor-corrector method of Nash (Ref. 12). Results from Whitfield's code (Ref. 5) show acceptable agreement with a multitude of boundary-layer data. The program is known by the acronym SWIM (Shear Work Integral Method).

The SWIM code provides a reasonable prediction of the flow separation, if separation is designated as the condition at which the numerical algorithm breaks down. The problem arises primarily because the boundary-layer equations are parabolic in nature and exhibit a singularity at separation (Ref. 13). Physically, this means the influence of the flow is felt only in the downstream direction. Therefore, after separation occurs, the flow information cannot influence the flow upstream, producing a singularity at the separation point.

Because of the importance of separated flows, work was needed to extend Whitfield's method to the separated flow regime. First, improvements to Whitfield's velocity profile correlation to include reverse flows were required. Swafford (Ref. 14) made improvements and succeeded in extending Whitfield's shape factor correlations and the skin friction correlation of White to the separated flow region.

Second, the singularity at the separation point needed to be eliminated. Catherall and Mangler report (Ref. 15) that the singularity may be removed by the specification of the displacement thickness (δ^*) or the wall shear distribution rather than a pressure distribution as in the SWIM code. The displacement thickness may be prescribed when the boundary layer is computed by the inverse method. Swafford's correlations reveal that when H becomes large enough (~ 3.2), a separated flow profile and a negative skin friction will emerge. A plot of the skin friction correlation is shown in Fig. 2. Because of the limited amount of experimental data available for separated flows, the correlations used in the separated regions cannot yet be considered universally applicable, especially for separated flows in which $\overline{H} \geq 4$. However, the correlations are generally considered good for $\overline{H} \leq 4$. The Cebeci-Smith turbulence model is retained for the separated region with the assumption that the turbulence model is valid in reverse flow. This is questionable since the turbulent energy production term is very small in a separated flow region. The outer portion of the boundary layer is still "wake-like," however.

The SWIM code has been altered (Ref. 4) to make use of the inverse method and was coupled with an Euler equation code to produce a steady, inverse viscous-inviscid interaction code. The interaction code works well for both attached and separated flow and many two-dimensional problems may now be solved. The interaction process will be discussed in more detail in Section 5.0.

3.2 UNSTEADY BOUNDARY-LAYER METHODS

An unsteady boundary-layer method based upon the principles used in the SWIM code and the separated flow correlations was devised by Whitfield. It solves the two-dimensional integral compressible, unsteady boundary-layer equations derived in Section 2.0. Time is an incremental stepping parameter in the formulation. Thus, the entire boundary layer is determined after each time step. It must be emphasized that the time-advancing routine is only a means of arriving at a final steady-state solution. Any solution in the interim is not representative of the real time flow. Hence, the temporal gradients are not necessarily correct.

The unsteady integral boundary-layer equations were formulated to be solved by the direct method (see Appendix A), in which surface pressures are used as input to the code.
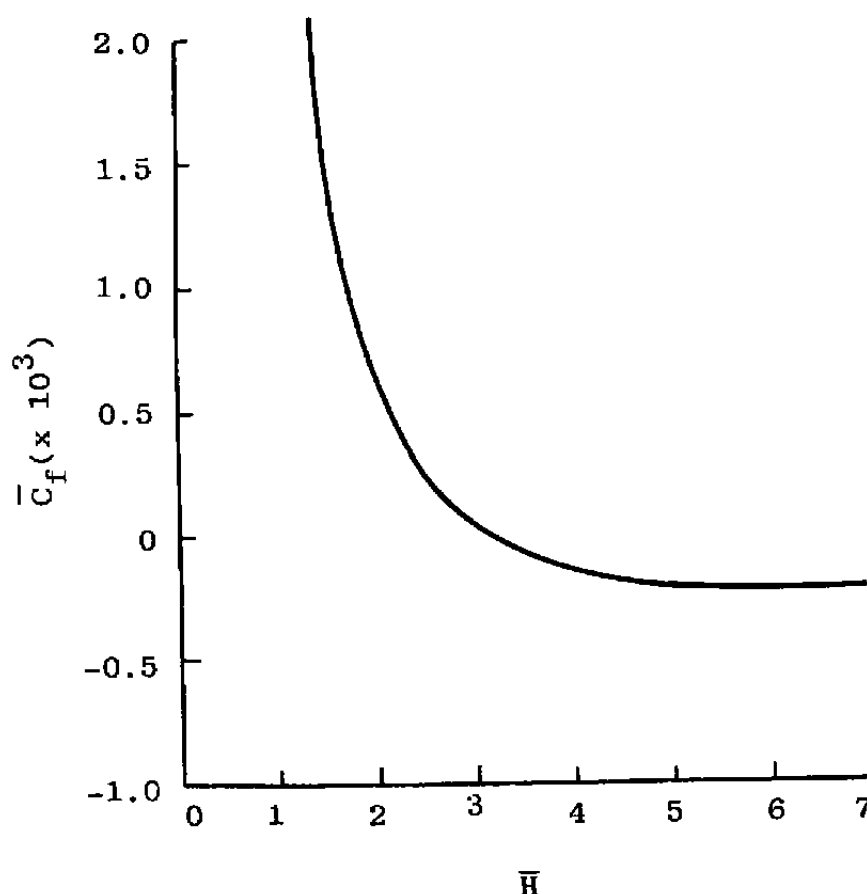
14

Figure 2. Correlation of incompressible skin friction, $\overline{c_f}$, for attached and separated flows.

The parameters computed from the solution process are the momentum thickness (θ) and the incompressible shape factor ($\overline{H}$). A flat plate approximation of the $\overline{\theta}$ and $\overline{H}$ distributions is used to begin the solution process. An additional shape factor (H_{θ_ρ}) correlation was required to solve the unsteady problem and was obtained in the same manner as the previous shape factor correlations. After each time step of the unsteady method, a new distribution of θ and $\overline{H}$ is determined on the entire body. The new distributions are used as an approximation for the next time step. The iteration process is continued until steady state is obtained. All other integral parameters may be computed by means of the shape factor correlations once distributions of Mach number and $\overline{H}$ are known. The Mach number is known from the input. The unsteady direct solution process is shown in Table 1.

Cousteix, et al. (Ref. 16) have suggested that singularities are possible with an unsteady direct method. Whitfield developed an inverse unsteady method to avoid such singularities, as was done in the steady version. The unsteady boundary-layer equations were formulated

Table 1. Solution Procedure for the Unsteady, Direct
Boundary-Layer Method

Step	Procedure
1.	Input initial values of H(x) and θ(x) distributions (flat plate approximations) and M_e(x).
2.	Evaluate all other parameters using H, M_e, and Re_θ at every spatial station.
3.	Solve equations for $\partial\theta/\partial t$ and $\partial H/\partial t$ at every spatial station.
4.	Compute θ, H at next time step (backward difference in time) at all spatial stations.
5.	Use θ, H distributions for next time step.
6.	Go to step 2 and do until convergence (where $\partial\theta/\partial t$ and $\partial H/\partial t \rightarrow 0$).

for the inverse method (see Appendix B) in which a δ^* distribution is used as input. The parameters to be determined by the time-dependent inverse solution process are θ and the edge velocity (u_e). As was done in the direct unsteady method, the two boundary-layer parameters (θ and u_e) which are obtained in the solution are updated in time until steady state is reached. The unsteady inverse process is shown in Table 2.

Whenever a δ^* distribution is not available, an inverse boundary-layer code may be used in a pseudodirect mode. Here, a pressure distribution is used as input and, by the iterative process of Carter discussed in Section 5.0, an initial δ^* distribution (using flat plate data, for example) may be updated until convergence. With each δ^* distribution during the solution process, a pressure distribution is obtained from the boundary-layer code and compared to the input value of pressure. The ratio of computed pressures to input pressures is used in Carter's method to update the next δ^* distribution. In this manner a pressure distribution is used as input, yet the inverse method is used to obtain a solution. This method is valid only for attached flows. It is not known why this method will not compute separated flows and an inverse method will. The pseudodirect method was used in the present work when comparisons between direct and inverse codes were made for attached flows.

Both the direct and inverse methods employ a fourth-order, variable step Runge-Kutta scheme in the solution processes. This method had the best convergence record with an upstream spatial differencing scheme. Central differencing was tried earlier and was found to converge with only about half the accuracy achieved with the upstream differencing.

Table 2. Solution Procedure for the Unsteady, Inverse Boundary-Layer Method

Step   **Procedure**

1. Input initial values of $\overline{H}(x)$ and $\delta^*(x)$ distributions (flat plate approximations) and $u_e(x)$ distribution from inviscid solution.

2. Evaluate all other parameters using $\overline{H}$, M_e, and Re_θ at every spatial station.

3. Solve equations for $\partial\theta/\partial t$ and $\partial u_e/\partial t$ at every spatial station.

4. Compute M_e and $\overline{H}$ from values of u_e, θ, and δ^* using backward differencing.

5. Use M_e and $\overline{H}$ distributions as approximations for next time step.

6. Go to step 2 and do until convergence (where $\partial\theta/\partial t$ and $\partial u_e/\partial t \rightarrow 0$).

4.0 DIRECT AND INVERSE UNSTEADY BOUNDARY-LAYER RESULTS

To choose the best unsteady method for coupling with the Euler code to obtain an unsteady viscous-inviscid boundary-layer code, both the direct and inverse unsteady methods were used to compute attached and separated boundary-layer flows. For attached flows the inverse code was run in the pseudodirect mode to use the same experimental pressure distributions as the direct method. This allows a more direct comparison between the two methods. For separated flows, the direct method uses the experimental pressure distribution while the inverse method uses the measured displacement thickness distribution.

The two attached flow cases considered (designated Case 6 and Case 9) are taken from Ref. 17 which includes boundary-layer data for an RAE 2822 airfoil at several Mach numbers and angles of attack. Case 6 and Case 9 upper surface measured pressure distributions were used as input for both codes and solutions were obtained for the boundary layers. The airfoil is equally divided into 150 increments in the present study and the pressure distribution was interpolated for each point to begin the solution. One hundred fifty increments have been found to be sufficient for describing a shock located on the airfoil. Both flow cases considered include a shock about mid-chord. Case 9 has the stronger shock. The codes provide a continuous solution through the shock region and no turbulence enhancement is made across the shock.

The various boundary-layer parameter distributions of Case 6 for both the direct and inverse solutions are given in Fig. 3. The two solutions are indistinguishable and both are

AEDC-TR-84-7
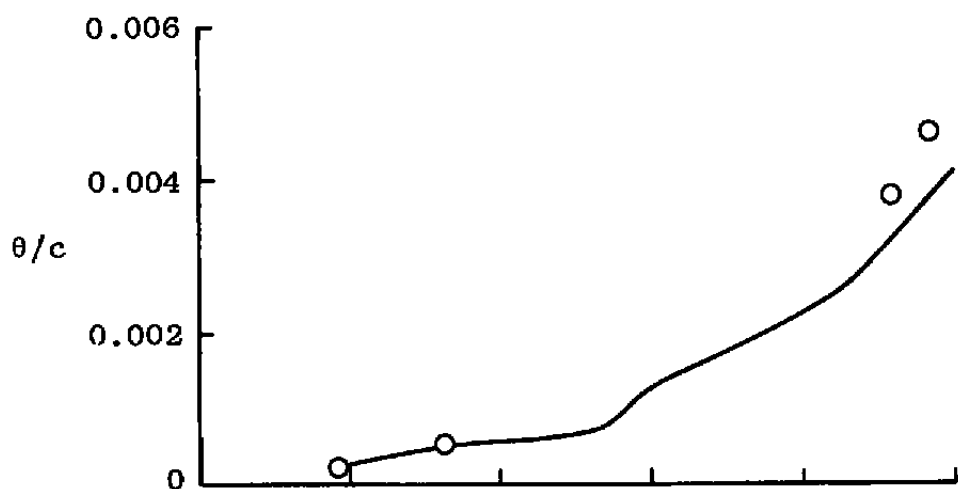
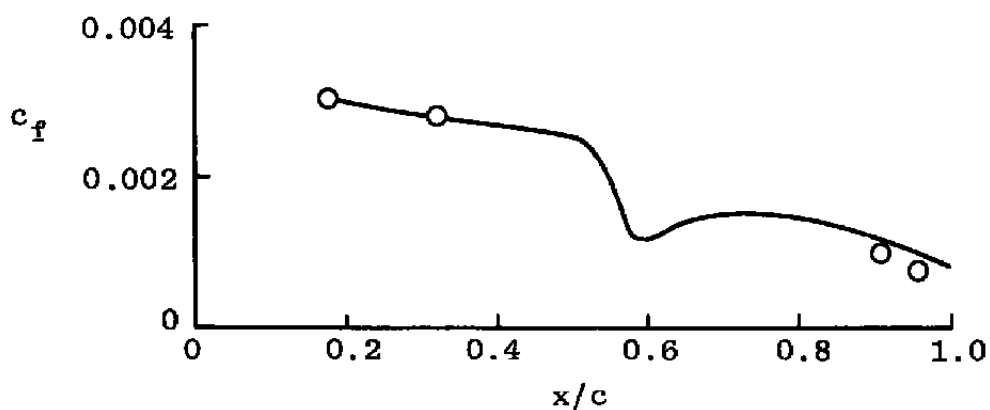RAE 2822 Airfoil (Upper Surface), Case 6

M = 0.725

α = 2.92 deg

Re/c = 6.5 x 10^6

Sym

O   Experiment

———   Unsteady Boundary-Layer Code (Direct and Inverse Methods)
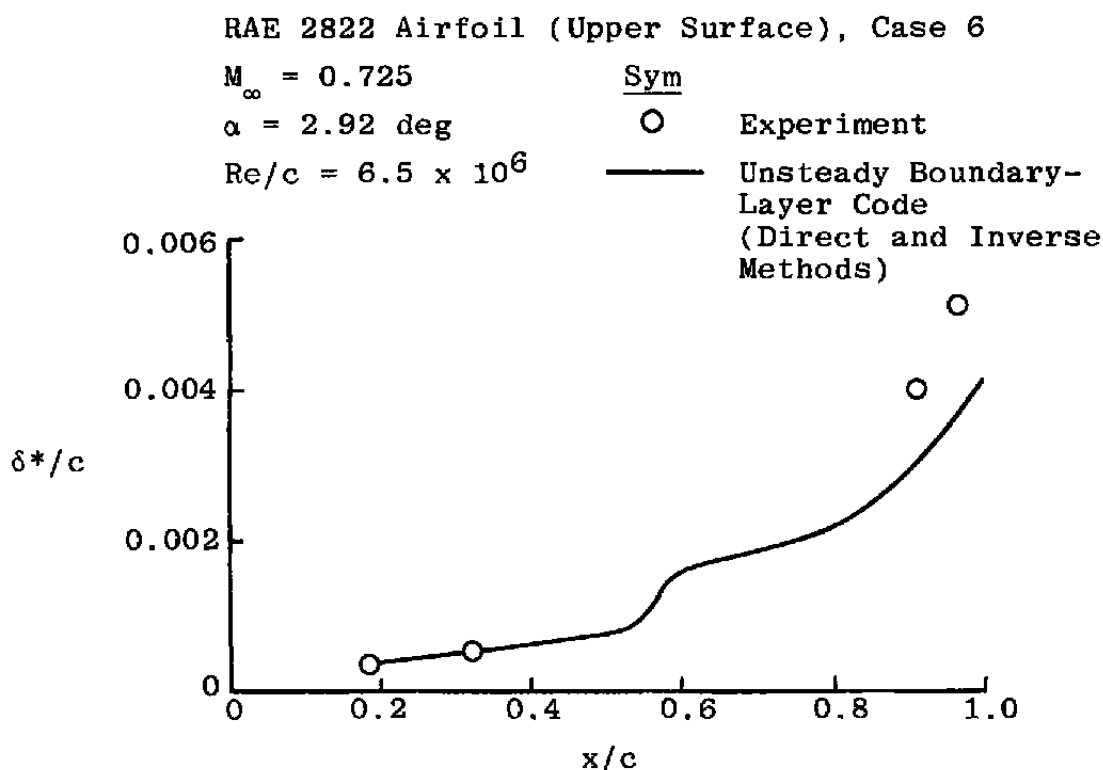
θ/c

a. Momentum thickness

c_f

x/c

b. Skin friction

Figure 3. Comparison of boundary-layer parameter measurements with the unsteady bounday-layer code for both direct and inverse methods (Case 6).

18

plotted as one line. The same pattern for Case 9 is shown by the solutions presented in Fig. 4. In both cases the shock location is clearly evident as an abrupt change in the boundary-layer parameters. When compared with available boundary-layer data (Figs. 3 and 4), the two techniques compare well upstream of the shock but fall below the data downstream of the shock. From experience with the steady flow codes, this result is not unusual when strong shocks are present. A possible reason for the discrepancy is that the shock may amplify the turbulence of the flow which is not considered in either the shear work integral or the skin friction equation of the present method.

RAE 2822 Airfoil (Upper Surface), Case 6

M_∞ = 0.725

α = 2.92 deg

Re/c = 6.5 x 10^6

Sym	
O	Experiment
——	Unsteady Boundary-Layer Code (Direct and Inverse Methods)

c. Displacement thickness
Figure 3. Concluded.

Two cases of low-speed separated flow data, compiled by Simpson, et al. (Refs. 18 and 19), were used to produce solutions by both the direct and inverse methods. The experimental displacement thickness distribution was used as input to the inverse method. Comparisons of both solutions with data are presented in Figs. 5 and 6. Flow separation (c_f = 0) was predicted by the inverse method for both cases of Simpson which was in agreement with the measured location. The direct method did not predict flow separation. Solutions by the inverse method do not agree well with momentum thickness data downstream of the separation point. This is probably because the shape factor correlations used are applied beyond their useful limits (that is, H > 4 occurs in the present case).

RAE 2822 Airfoil (Upper Surface), Case 9

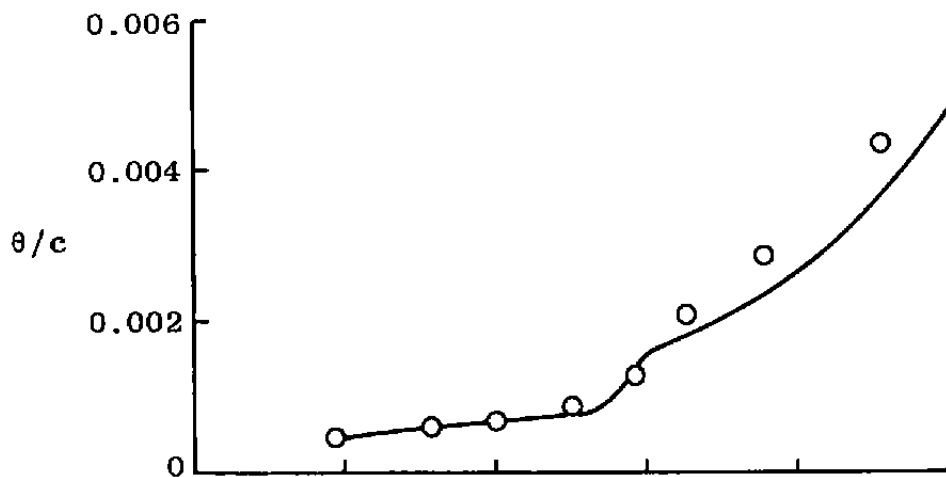M_∞ = 0.734

α = 3.19 deg
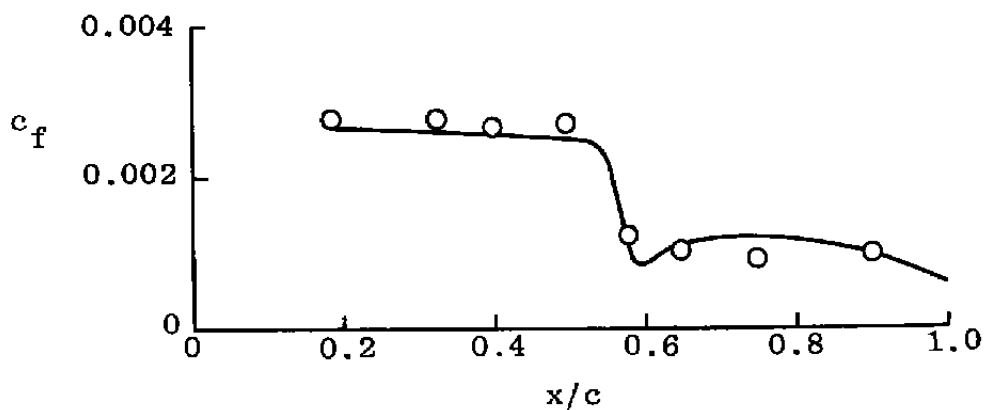
Re/c = 6.5 x 10^6

Sym

O   Experiment

——— Unsteady Boundary-
     Layer Code
     (Direct and Inverse
     Methods)

a. Momentum thickness

b. Skin friction

Figure 4. Comparison of boundary layer parameter measurements
with the unsteady boundary layer code for both direct
and inverse methods (Case 9).
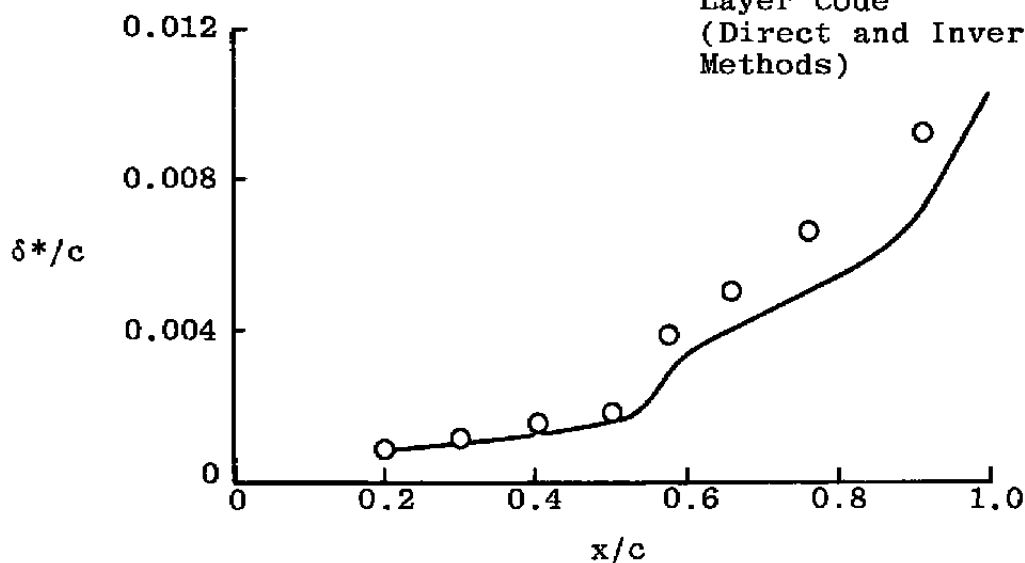
RAE 2822 Airfoil (Upper Surface), Case 9

M_∞ = 0.734

α = 3.19 deg

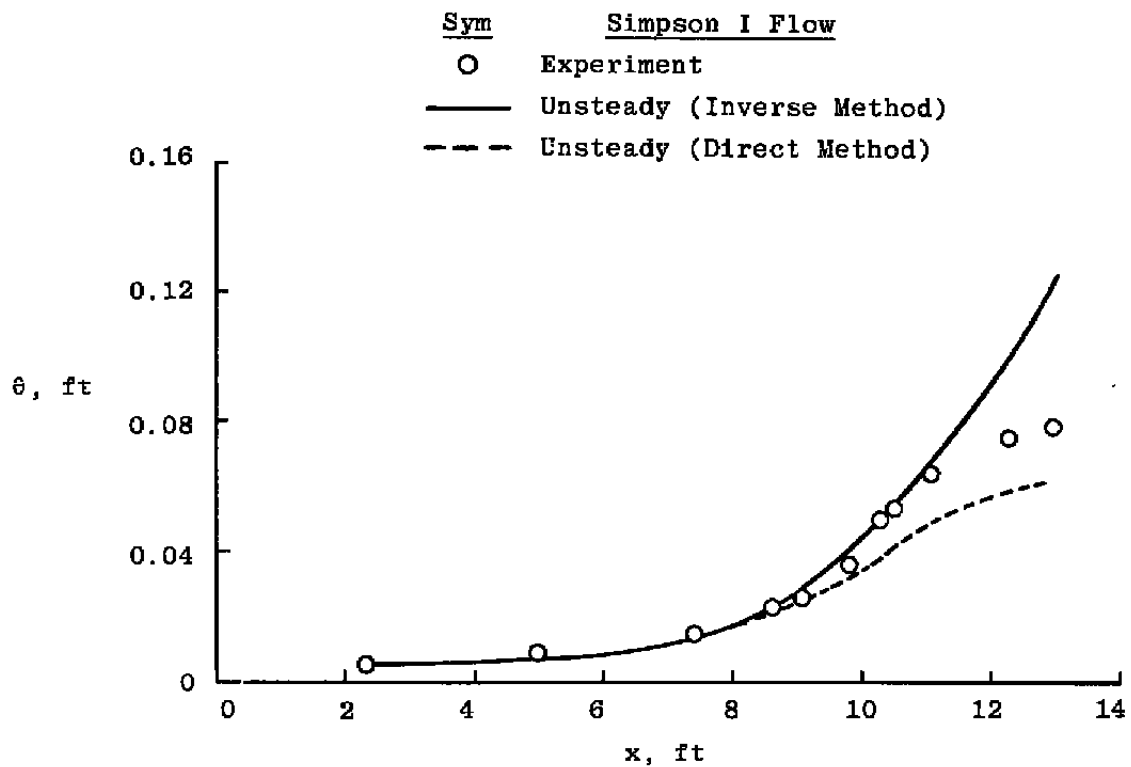Re/c = 6.5 x 10^6

<u>Sym</u>

O   Experiment

——   Unsteady Boundary-Layer Code (Direct and Inverse Methods)
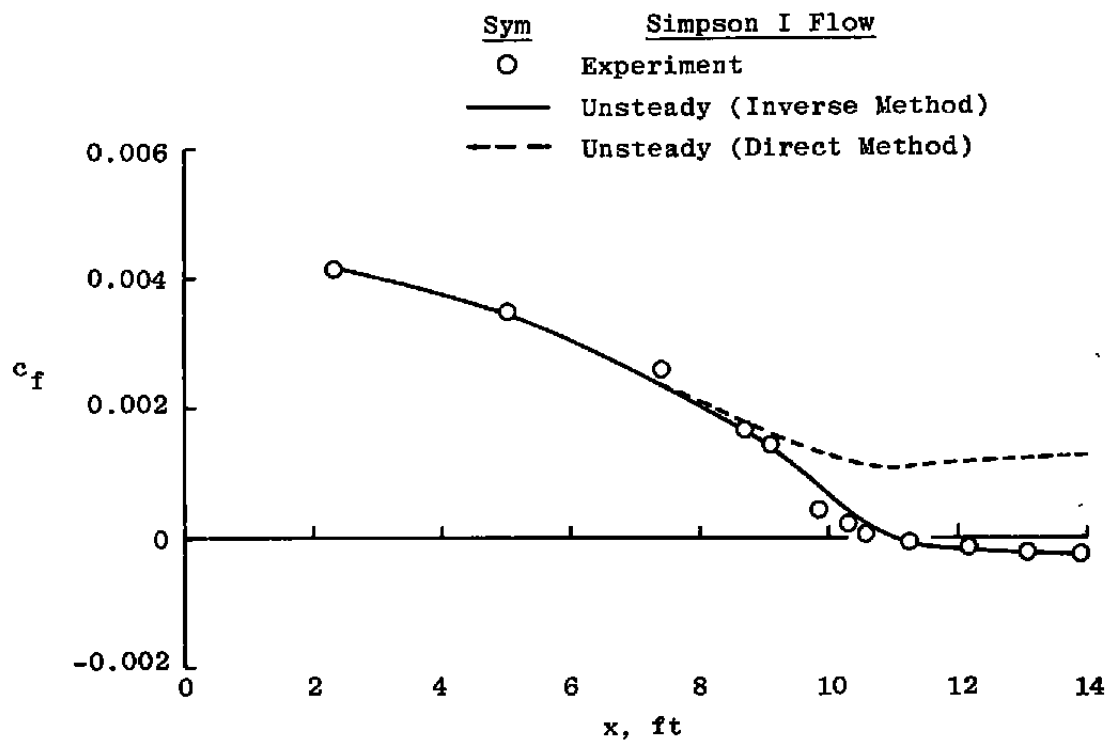

c. Displacement thickness

Figure 4. Concluded.

a. Momentum thickness

Figure 5. Comparison of boundary-layer parameter measurements of
separated flow with the unsteady boundary-layer code for
both direct and inverse methods (Simpson I).
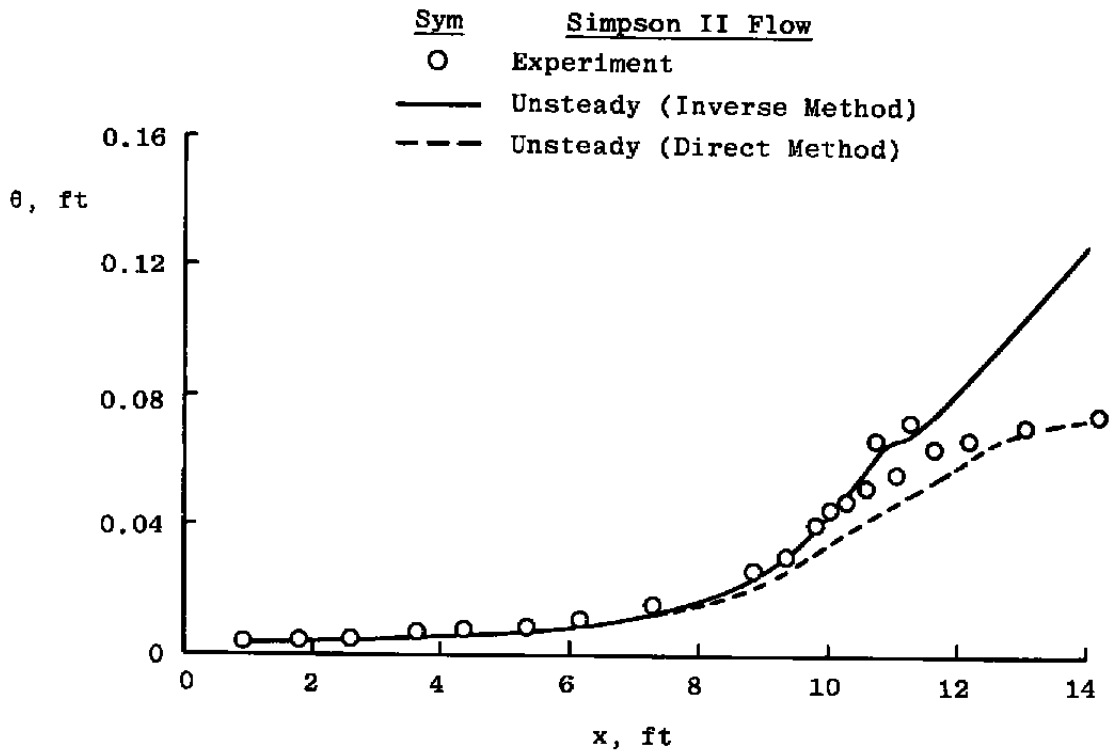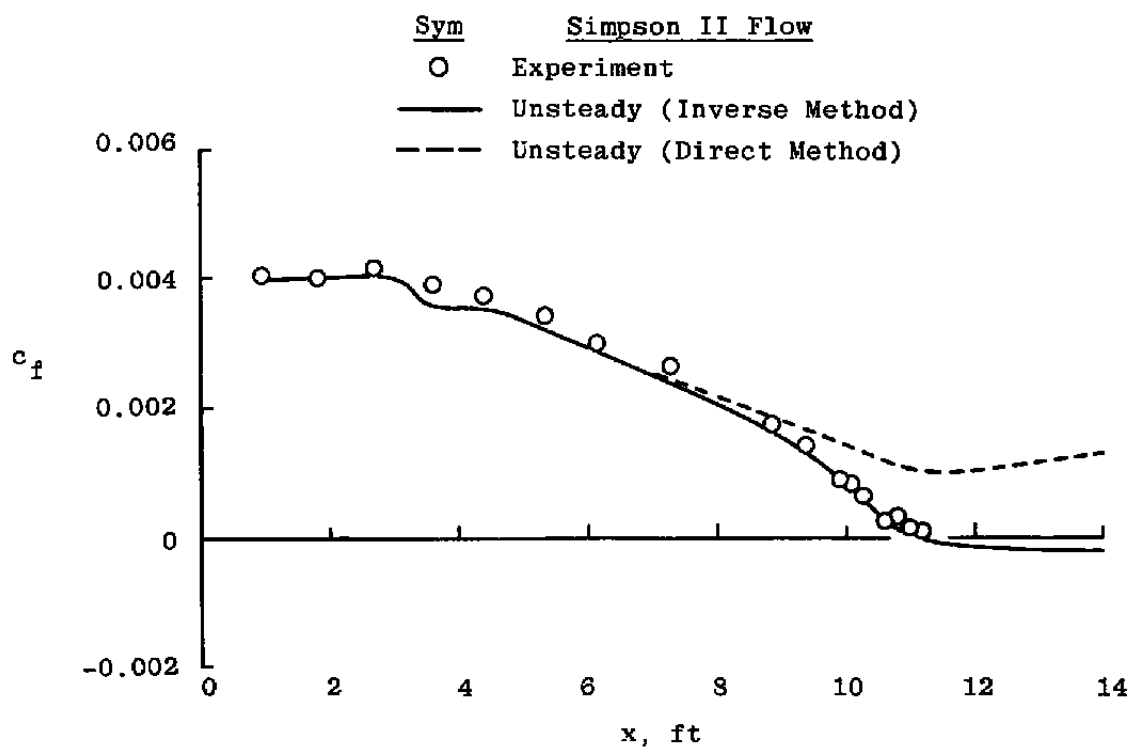
b. Skin friction

Figure 5. Concluded.

a. Momentum thickness

Figure 6. Comparison of boundary-layer parameter measurements of separated flow with the unsteady boundary-layer code for both direct and inverse methods (Simpson II).

b. Skin friction
Figure 6. Concluded.

Two important points are made from the unsteady boundary-layer results. First, both the direct and inverse method produce comparable solutions for attached flows. Second, the inverse method will compute a separated flow solution, whereas the direct method will not. The results justify coupling the inverse boundary-layer method with an Euler equation code to create an unsteady interaction code capable of solving flows with separation. This task is the focus of the present work.

5.0 TRANSONIC VISCOUS-INVISCID INTERACTION METHOD

5.1 INTERACTION PROCESS

The successful application of the inverse unsteady boundary-layer code in conjunction with an Euler code would greatly enhance the progress being made to compute three-dimensional viscous-inviscid interacting flows. The applications would verify that the unsteady interaction methodology, which is the technique to be used in three-dimensional computations, is feasible.

The interaction process used in the steady interaction code is the same one employed by the unsteady formulation. The overall interaction scheme is based upon computing the Euler equations for several time iterations, then employing the viscous method, and continuing this viscous-inviscid loop until steady state is obtained. The unsteady Euler equations are hyperbolic; thus, every point in the flow field influences other points via the domain of influence in the time plane as dictated by the characteristics. This property aids in distributing the effects of the boundary layer to the rest of the flow field.

Whitfield's steady interaction method applies the surface source model of Lighthill (Ref. 20) as a coupling device between the viscous and inviscid computational regions. This choice permits the inviscid computational mesh to remain fixed. The surface source model imposes a mass flux on the airfoil of the form

$$(\varrho v)_n = \frac{d}{dx} (\varrho_e u_e \delta^*), \tag{30}$$

where $(\varrho v)_n$ is the local mass flux normal to the surface and numerically simulates the displacement effect caused by the boundary layer.

Physically, the surface source term may be compared to a blowing effect which mimics the boundary-layer displacement. There continues to be a conservation of mass within the computational domain by solution of the continuity equation. Mass entering from the body is a boundary influx and a momentum source, as at the entrance plane, and is matched by an additional outflux of mass at the flow exit plane. The added mass from the airfoil displaces

the effective body for the inviscid flow calculations. However, the net mass added in the boundary layer and wake is not zero and a global mass balance is not satisfied. Global momentum considerations then show that a thrust must be exerted on the airfoil. Since some of the added mass in the boundary layer is removed by sinks in the wake, the total mass addition is small. The scheme adopted here is similar to the method in which the displacement thickness is added to the airfoil for each new inviscid calculation. However, the present method has the advantage that the computational mesh never has to be altered.

After the flux term, $(\varrho v)_n$, is evaluated in each pass through the boundary-layer routine, it is transferred to the Euler code as an updated boundary condition on the body surface. During solution of the Euler equations, the flux term is held constant until the next boundary-layer calculation. Since the computations were made for airfoils, the upper and lower surfaces were computed separately within the boundary-layer routine.

In each viscous-inviscid cycle the displacement thickness distribution (initially assumed as a flat plate approximation) is updated by information from the previous viscous-inviscid cycle. This is done after the Euler equations are computed for several time cycles and before the boundary layer is computed again. The method used to specify the updated δ^* distribution is Carter's method (Ref. 21), which may be written as

$$\delta^{*(n+1)} = \delta^{*(n)} + \delta^{*(n)} \omega(u_{e,v}/u_{e,i} - 1), \tag{31}$$

where $\delta^*(n+1)$ is the updated displacement thickness; $\delta^*(n)$ is the displacement thickness from the previous viscous-inviscid cycle; $u_{e,v}$ is the local edge velocity obtained from the latest boundary-layer solution; $u_{e,i}$ is the velocity obtained from the previous Euler equation solution; and ω is the relaxation parameter. Details of the boundary conditions in the Euler code are discussed in Section 5.2. The entire solution cycle of the Euler code and the boundary-layer routine is continued until the δ^* distribution is converged. The term $u_{e,v}/u_{e,i}$ which approaches unity during convergence is monitored as the convergent parameter. An interaction code of this type may produce better solutions than an integral boundary-layer code alone, especially if shocks are present in the flow. While the flow, including the shock, is being developed by the Euler code, the boundary layer is continuously interacting and periodically being updated, which allows the boundary layer to be coupled with the outer flow.

The unsteady integral boundary-layer code presented in Section 3.0 was essentially exchanged with the steady boundary-layer portion of the steady interaction code, creating an unsteady interaction code. After the exchange was accomplished some alterations were needed to successfully run the unsteady interaction code. In the steady interaction code, the incompressible shape factor $(\overline{H})$ was computed directly by the steady boundary-layer solution as was the edge Mach number. Since all correlations are based upon these two

parameters, any other parameter required in the solution process was easily obtained. After each boundary layer was completed, the $\overline{H}$ distribution was saved and used in the next viscous-inviscid cycle as a new approximation. The Mach number distribution was obtained from the Euler solution before each boundary-layer calculation.

However, the parameters computed directly by the unsteady boundary-layer solution are θ and edge velocity (u_e). After each viscous cycle, the θ distribution is saved for the next viscous-inviscid interaction. The $\overline{H}$ distribution is determined from the computed θ and the updated δ^* distribution (obtained by Carter's method). After the $\overline{H}$ distribution has been determined, the other parameters required for the viscous solution process may be computed from the shape factor correlations and edge Mach number as before.

Another problem associated with the unsteady interaction code is the time-stepping iterations of the viscous part of the code. The steady viscous solution is marched spatially along the body, while in the unsteady viscous method, a number of time iterations must be completed within each boundary-layer calculation. The most economical process for the present cases was to begin with a few iterations (usually 50) within the boundary-layer solution and arbitrarily increase the number of viscous iterations with each viscous-inviscid loop. The last time the boundary layer was computed, the number of viscous iterations was arbitrarily set at 500 time steps. This made a total of 4,000 to 5,000 time steps within the viscous part of the code. Also, a total of approximately 1,000 time steps was required in the inviscid part of the code. If no boundary layer were computed, the Euler code still requires approximately 1,000 iterations for convergence of the flow cases presented here.

5.2 EULER EQUATION CODE

The Euler code used in the present work in conjunction with the inverse unsteady boundary-layer code was developed by Jameson and is fully described in Ref. 6. The code is written in full conservation form and allows the representation of shocks and other discontinuities in flows over airfoils. Far field boundary conditions allow either subsonic or supersonic flows. All solid surface boundary pressures are extrapolated from the flow field values. When effects of the boundary layer are added to the Euler code, the flux term associated with the growth in the displacement thickness is included at the solid surface. The method of solving the time-dependent Euler equations is a four-equation, fourth-order Runge-Kutta scheme with local time stepping and central spatial differencing.

A C-mesh is used in the Euler code (Fig. 7) because it is considered best for airfoil solutions in which the wake region is computed because it allows a dense spacing in the wake region. The spacing of the mesh for the two-dimensional cases considered in the present work was 127 by 31 with 45 points on each of the airfoil upper and lower surfaces. The mesh
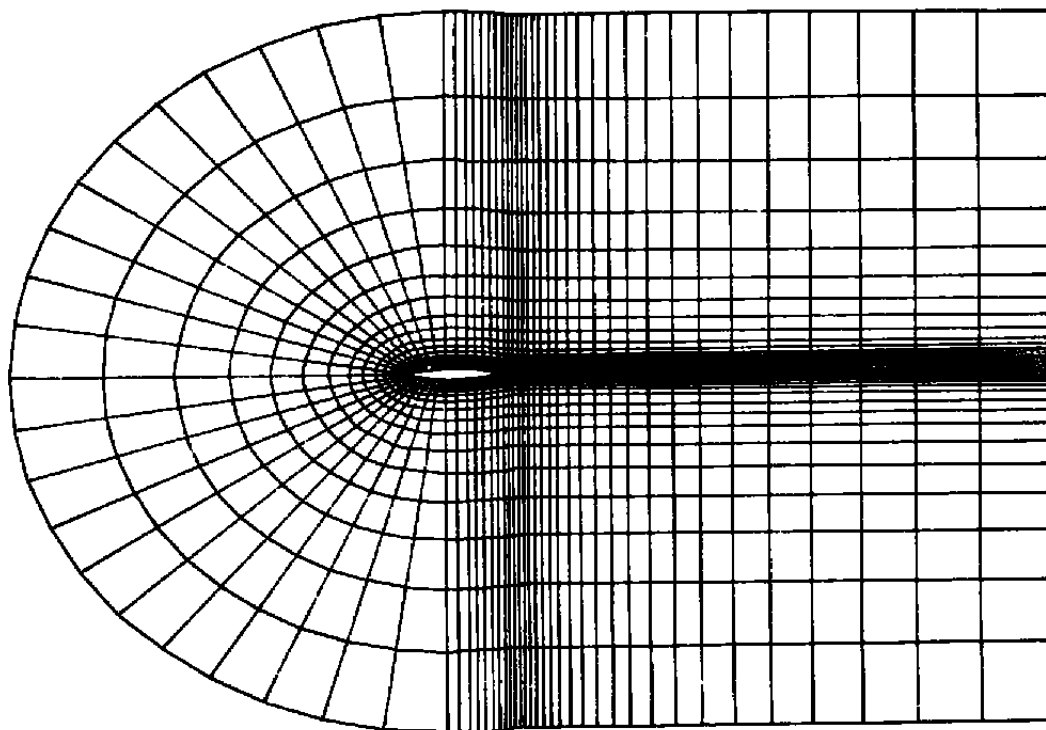
Figure 7. Representative sample of a C-type mesh about an airfoil.

may also be aligned, if desired, with possible discontinuities such as shocks or slipstreams in the flow field. No changes in the inviscid mesh are required for applying the viscous effects of the boundary-layer code, and no interpolations are needed. The mesh remains fixed in time. These features will be significant factors when the viscous-inviscid method is extended to three- dimensional problems.

Viscous solutions of the wake region in viscous-inviscid iterations are computed by establishing a small value (10^{-6}) for the skin friction and applying the boundary-layer code for the wake as an extension to the airfoil surface. The wake boundary condition is linearized; i.e., is applied along the centerline of the mesh downstream of the airfoil. Although the boundary condition is not applied at the real wake location, the slipstream camber, which results from the solution of the code, is computed at the correct location. A fair representation of the wake may be made in this manner.

Boundary conditions required in the Euler code include specific inflow and outflow conditions for either subsonic or supersonic flows at the far field boundary. Inflow conditions for supersonic flow are set to free-stream values and outflow parameters are extrapolated from the interior values. For subsonic inflow conditions, the density is determined by extrapolation while other properties of the flow are evaluated from the

29

density and stagnation conditions. Pressure is set to the free-stream value as a subsonic outflow condition while velocities are obtained by extrapolation. All other flow parameters may be determined when these far field properties are set.

5.3 RESULTS OF THE STEADY AND UNSTEADY VISCOUS-INVISCID INTERACTION CODES

Results of the unsteady interaction code developed in the present work and results of the steady interaction code of Ref. 4 are discussed and compared with data. Three sets of data are considered. Case 6 and Case 9 (Ref. 17) of Section 4.0 were computed with both interaction codes. Another data case from the same reference (denoted Case 3) is also considered. The results are presented in two parts. The first includes comparisons of pressure coefficient data with computations (Figs. 8, 9, and 10); the second contains comparisons of the boundary-layer data with computations (Figs. 11, 12, and 13). Since no lower surface boundary-layer data were reported, only the Case 9 lower surface computations are presented (Fig. 14) to show that the trends are reasonable.

For all three cases the point of origin of the boundary layer is at 18-percent chord. For these highly loaded aft-end airfoils it is essential that the effective camber over the last 20 percent or so of the airfoil be estimated correctly. The fixing of the boundary layer at 18-percent chord does not allow the boundary layer to adjust to stagnation point movement. In addition, the lower surface boundary layer may not be predicted too well in the strong adverse pressure gradient downstream of 50-percent chord.

The predicted pressure distribution for Case 3 is compared to data for both the steady and unsteady interaction code results in Fig. 8. Both computations produce essentially the same distributions and are presented as a single curve. The comparison with data is considered good except on the upper surface ahead of the 10-percent chord position. Such a discrepancy occurs with many airfoil calculations and is related to the lack of mesh resolution near the leading edge. The lower surface pressures are slightly underpredicted. If the flow is supercritical, the introduction of the boundary layer at 18-percent chord causes a jump in the pressure distribution at that point which can result in small changes in lift attributable to the differential boundary-layer growth resembling a camber change to the airfoil. There is also a thickness discontinuity at the location at which the boundary layer is introduced.

Case 6 and 9 pressure coefficient comparisons are shown in Figs. 9 and 10. The difference between the steady and unsteady calculations is apparent. Both methods provide reasonably good results when compared to data, and only a slight shift in the shock locations between the two methods is evident. Again, the largest discrepancy occurs in the pressure distributions of the lower surface and the initial 10-percent of the upper surface. The main point to be observed is that the steady and unsteady interaction codes agree well. In all three cases, the two codes give equally good surface pressure predictions.

Comparisons of the computed and measured upper surface boundary-layer quantities for Cases 3, 6, and 9 are presented in Figs. 11, 12, and 13. The parameters of interest are the displacement thickness (δ^*), momentum thickness (θ), and local skin friction (c_f). The pressure distribution calculations are shown as an aid in locating the shock position. Case 3 and 6 computations (Figs. 11 and 12) show good agreement between both methods for all three parameters. In the last 20-percent chord in both cases, computations and data have a larger discrepancy than at the upstream positions. Computations of Case 9 (Fig. 13) provide the best agreement with the data. Near the trailing edge, good predictions are made by both the steady and unsteady interaction codes. A strong shock is predicted by theory, but not enough data points are available in the boundary layer to determine the strength. However, the predicted shock location and strength are in good agreement, Fig. 10. As shown by the skin friction curves, both computations predict a near separation region just aft of the shock and near the trailing edge. The two computational methods agree well with each other.

Several assumptions made in either method may have resulted in the differences denoted between data and the analytical solutions. Assuming that the data are not influenced by extraneous factors, the integral method, which eliminates turbulence structure in the momentum equation and the simplistic turbulence model used in the shear work integral term, may be contributing factors to the differences. However, the overall results are good.

Figure 8. Comparison of the measured pressure distribution for Case 3 with the unsteady and steady interaction codes.

RAE 2822 Airfoil, Case 6

M_∞ = 0.725

α = 2.92 deg

Re/c = 6.5 x 10^6
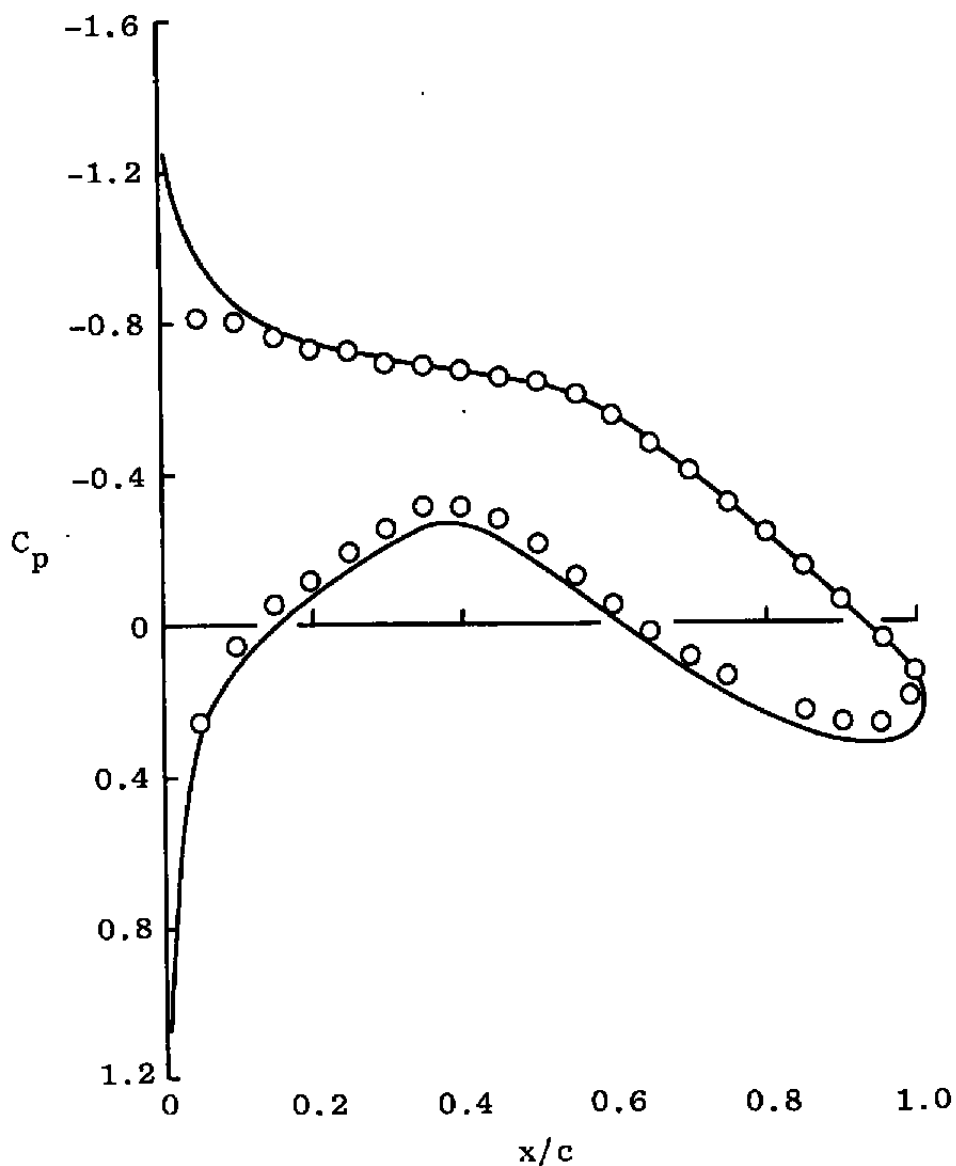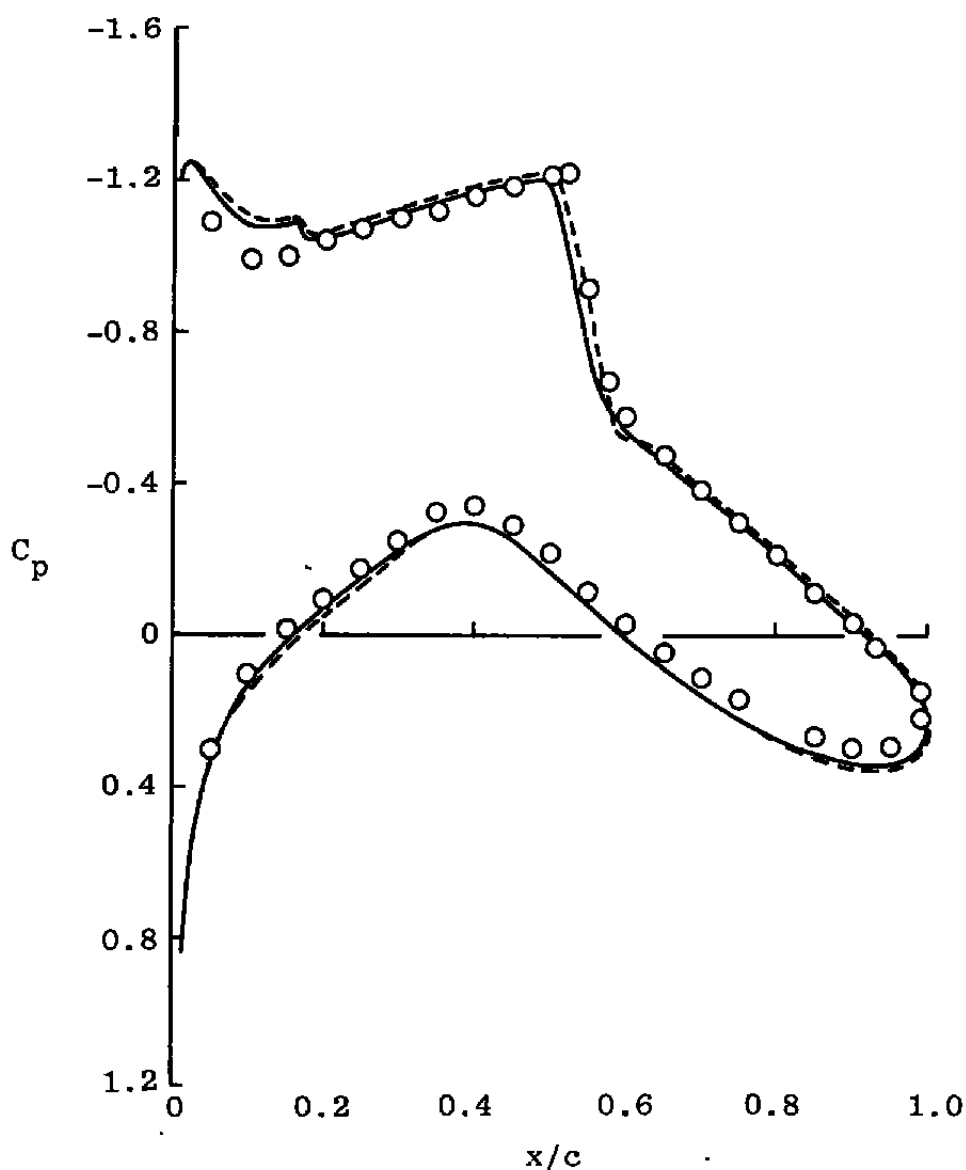
Sym

O   Experiment

———— Unsteady Interaction

— — — Steady Interaction

Figure 9. Comparison of the measured pressure distribution for Case 6 with the unsteady and steady interaction codes.

RAE 2822 Airfoil, Case 9

M_∞ = 0.734   <u>Sym</u>

α = 3.19 deg   O   Experiment

Re/c = 6.5 x 10^6 —— Unsteady Interaction

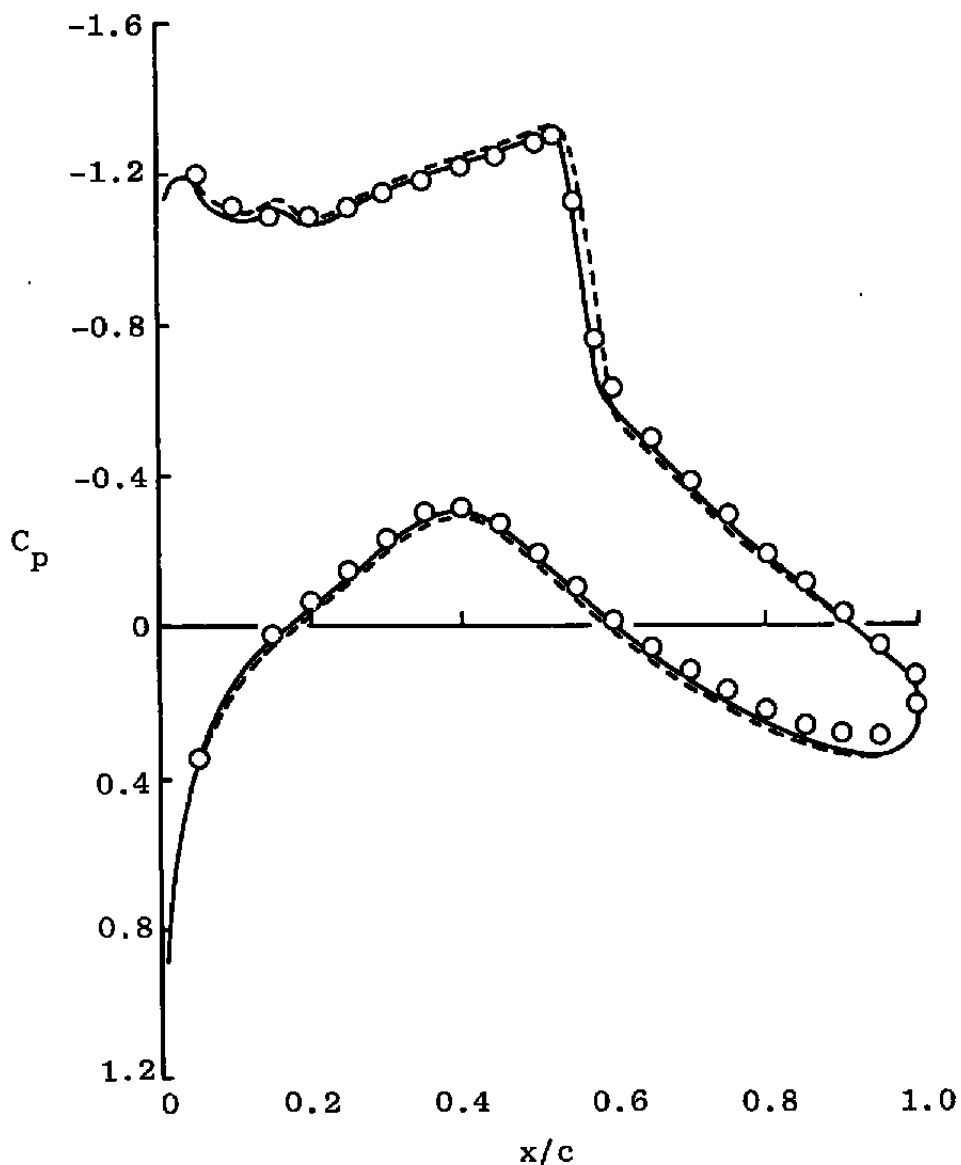   — — Steady Interaction

Figure 10. Comparison of the measured pressure distribution for Case 9 with the unsteady and steady interaction codes.

RAE 2822 Airfoil (Upper Surface), Case 3
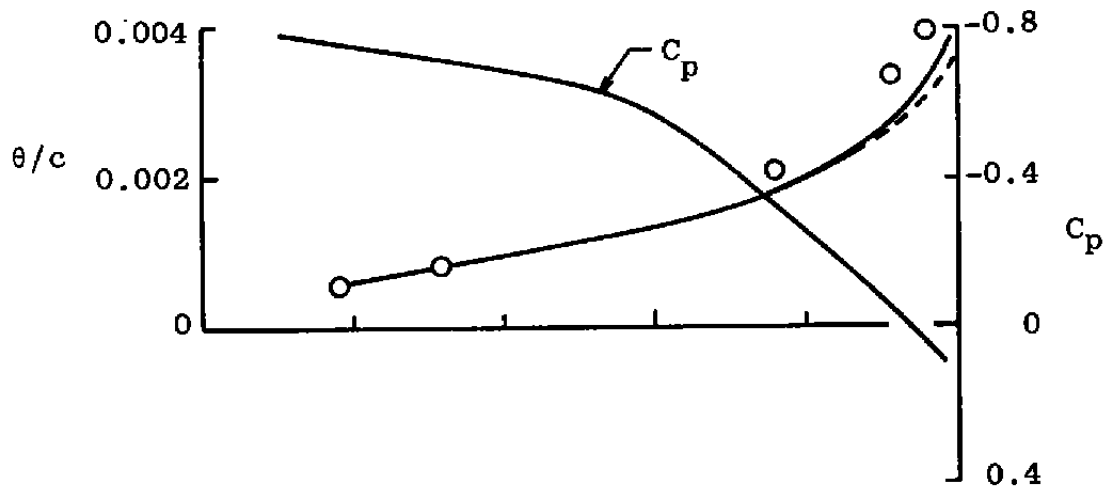
M_∞ = 0.60

α = 2.57 deg

Re/c = 6.3 x 10^6

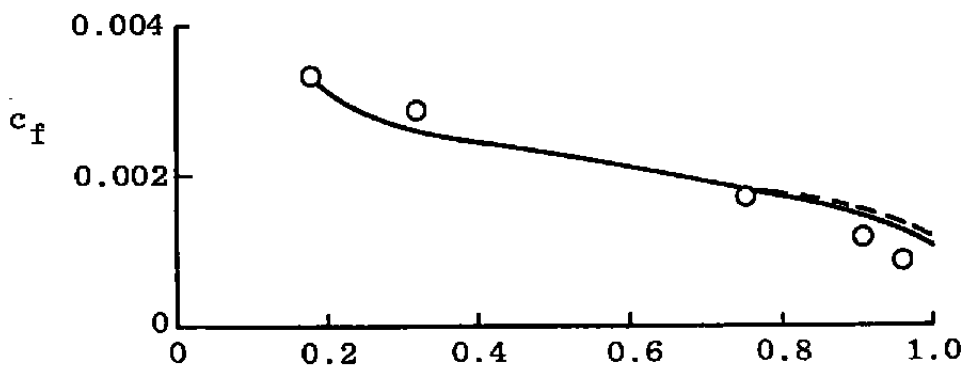| Sym	
O	Experiment
——	Unsteady Interaction
– – –	Steady Interaction

a. Momentum thickness

b. Skin friction

Figure 11. Comparison of measured upper surface boundary-layer parameters with calculations of the unsteady and steady interaction codes (Case 3).

RAE 2822 Airfoil (Upper Surface), Case 3

$M = 0.60$ <u>Sym</u>

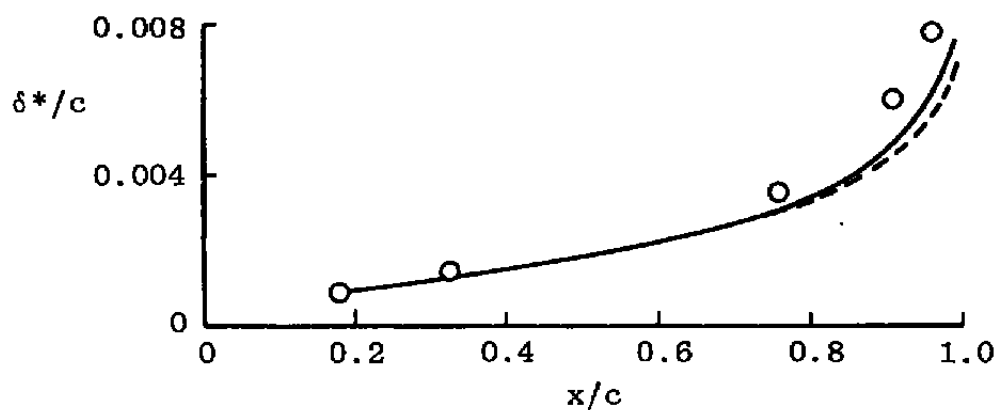$\alpha = 2.57$ deg   O   Experiment

$Re/c = 6.3 \times 10^6$ ——— Unsteady Interaction

                        — — — Steady Interaction

c. Displacement thickness
Figure 11. Concluded.

a. Momentum thickness

b. Skin friction

Figure 12. Comparison of measured upper surface boundary layer parameters with calculations of the unsteady and steady interaction codes (Case 6).

RAE 2822 Airfoil (Upper Surface), Case 6

$M_\infty = 0.725$

$\alpha = 2.92$ deg

$Re/c = 6.5 \times 10^6$

Sym	
$\bigcirc$	Experiment
——	Unsteady Interaction
— — —	Steady Interaction

c. Displacement thickness

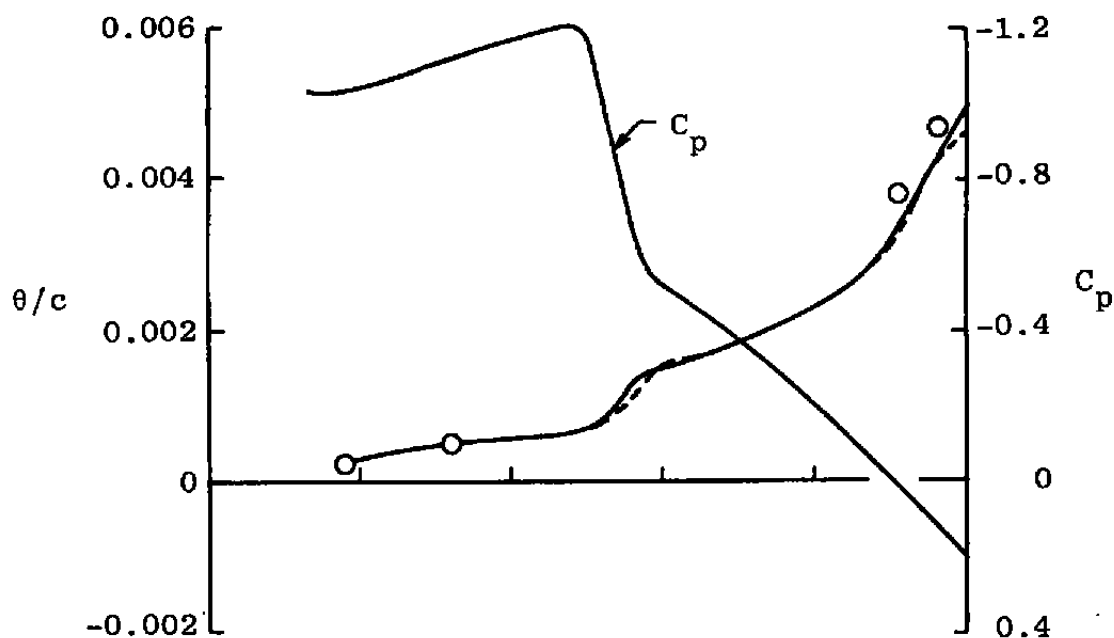Figure 12. Concluded.

RAE 2822 Airfoil (Upper Surface), Case 9

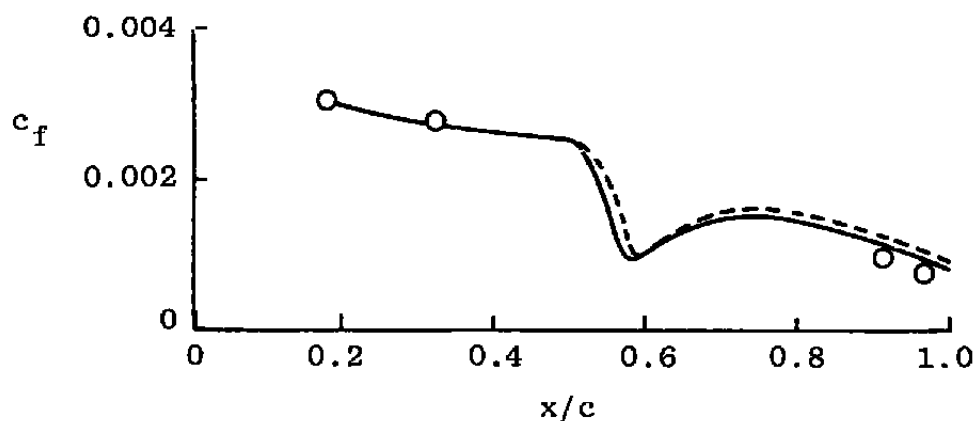M_∞ = 0.734   <u>Sym</u>

α = 3.19 deg   O   Experiment

Re/c = 6.5 x 10^6 —— Unsteady Interaction

                — — — Steady Interaction
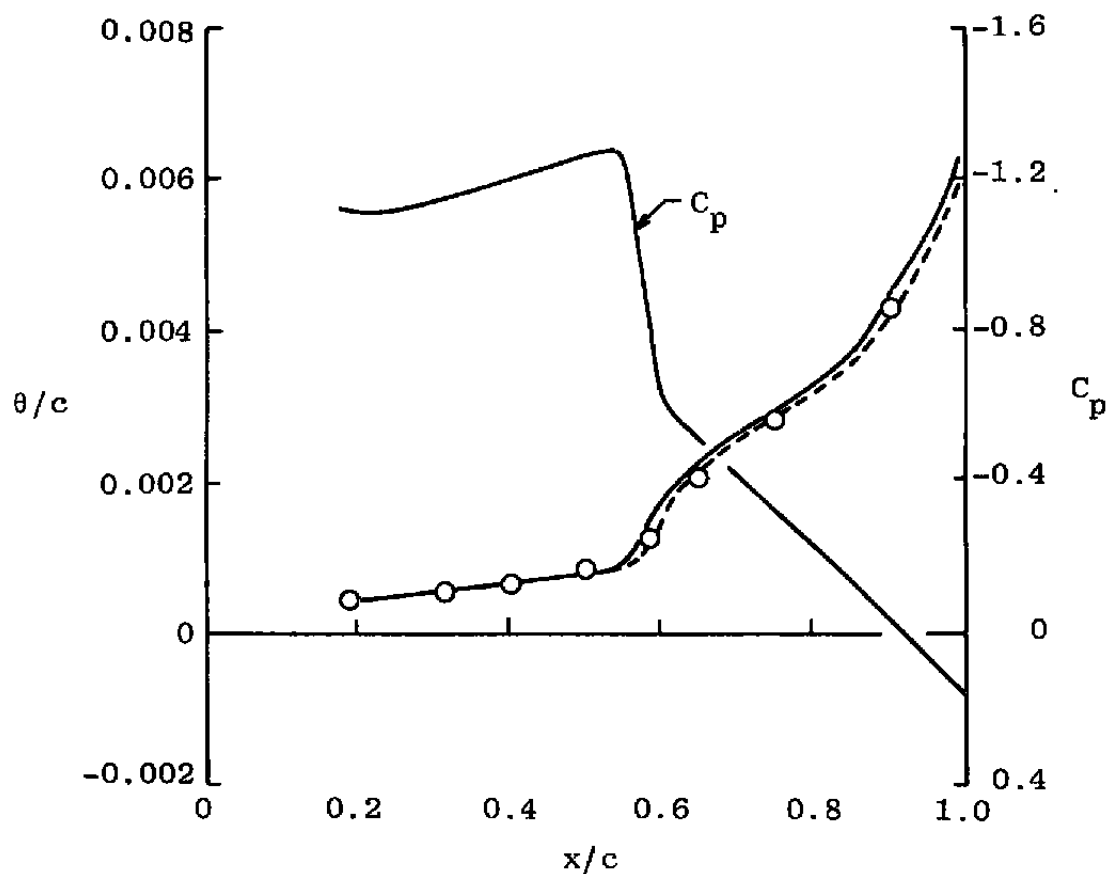
a. Momentum thickness

Figure 13. Comparison of measured upper surface boundary-layer parameters with calculations of the unsteady and steady interaction codes (Case 9).

RAE 2822 Airfoil (Upper Surface), Case 9

M = 0.734

α = 3.19 deg

Re/c = 6.5 x 10^6

Sym	
O	Experiment
——	Unsteady Interaction
— — —	Steady Interaction

b. Skin friction

Figure 13. Continued.

RAE 2822 Airfoil (Upper Surface), Case 9

M∞ = 0.734
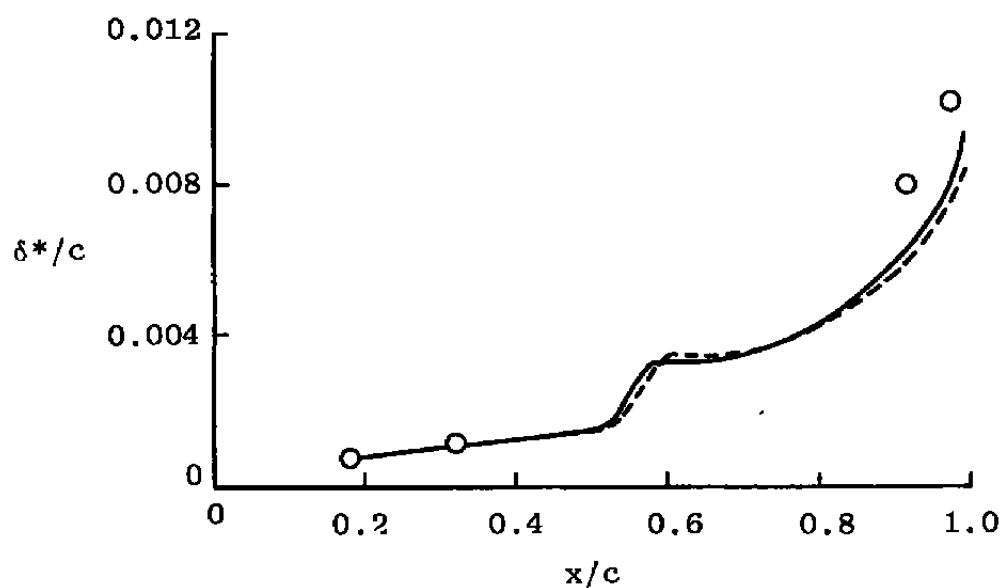
α = 3.19 deg

Re/c = 6.5 x 10^6

Sym

○   Experiment

———   Unsteady Interaction

— — —   Steady Interaction
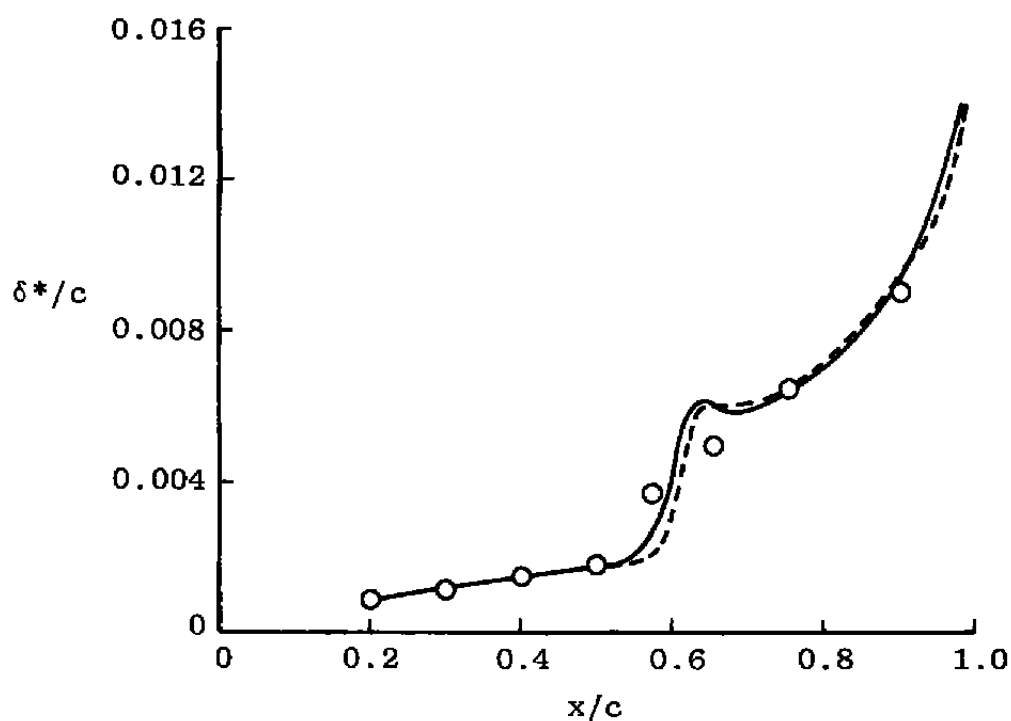
c. Displacement thickness

Figure 13. Concluded.

RAE 2822 Airfoil (Lower Surface), Case 9

$M_\infty = 0.734$ Sym

$\alpha = 3.19$ deg   ———— Unsteady Interaction

$Re/c = 6.5 \times 10^6$ — — — Steady Interaction

c. Displacement thickness
Figure 14. Concluded.

6.0 CONCLUSIONS AND RECOMMENDATIONS

The objective of this work was to produce and validate an unsteady viscous-inviscid interaction routine based upon a two-dimensional, unsteady integral compressible boundary-layer method devised by Whitfield and the Euler equation code developed b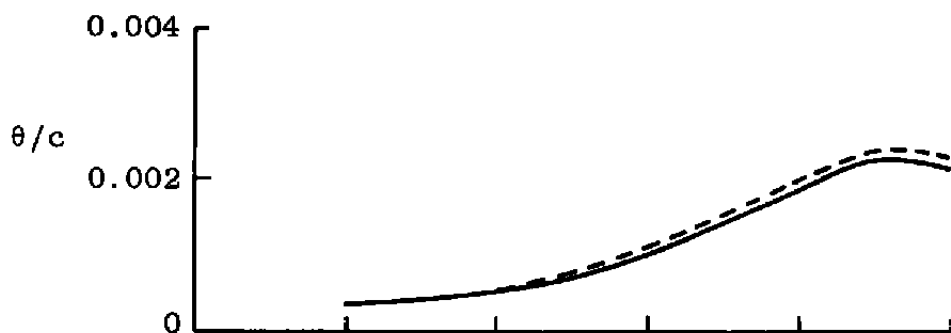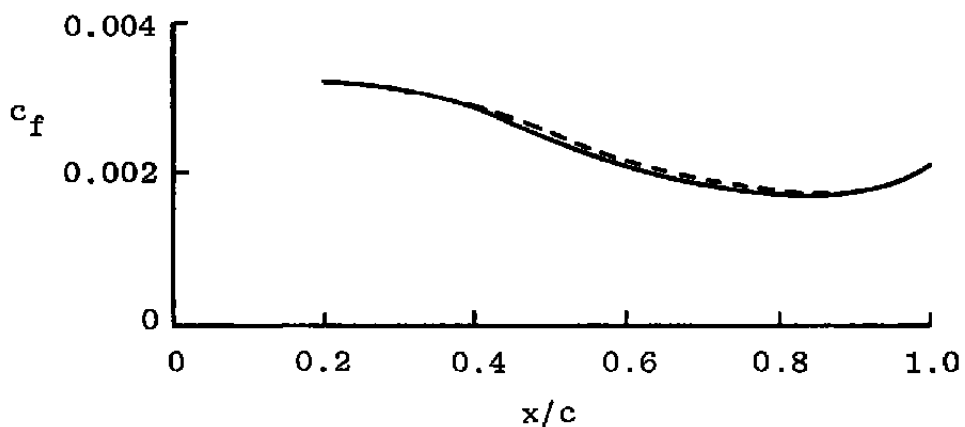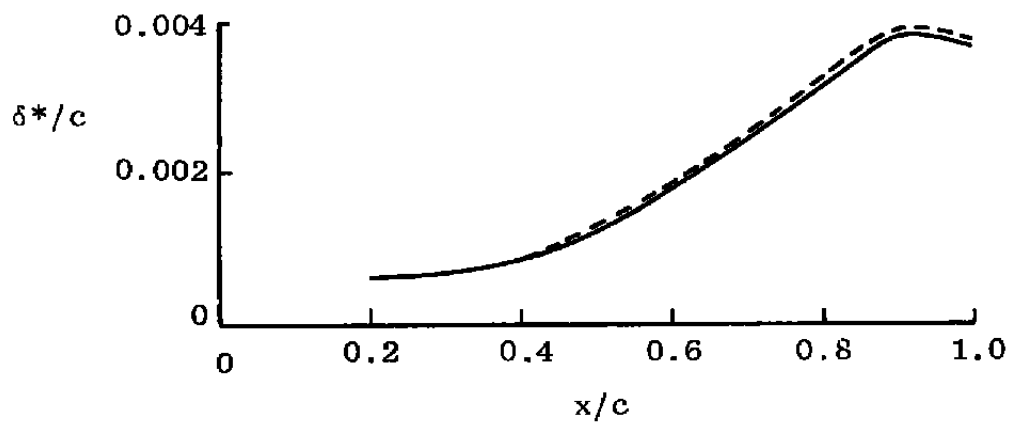y Jameson. The unsteady interaction code was compared with experimental data and with a steady viscous-inviscid interaction code which utilizes a steady integral boundary-layer method. The results indicate that the unsteady interaction method gives satisfactory answers.

The major advantage of the present work is that the method is computationally faster than a Navier-Stokes solution while providing good engineering solutions for transonic airfoil flows. Another advantage of the method is that the inviscid and viscous parts of the code both use the same computational mesh spacing in the streamwise direction.

The major disadvantage of the method is the use of a simplistic turbulence model within the calculations. Although this is one reason for the speed of the method, the turbulence modeling at a shock location, for example, could be improved.

To improve upon the present method, the time-dependent terms, which are set to zero, should be better approximated. This may lead to an accelerated convergence and more accurate solutions. Further testing of the interaction code should also be done to include wider ranges of Mach number and incidence. Also, cases in which separation is known to occur should be computed to provide information about the method's ability to predict separation.

Finally, the method should be extended to three dimensions to determine the difficulties that may arise. Once accomplished, a three-dimensional interaction code can be developed to compute viscous-inviscid solutions of realistic configurations in transonic flows.

REFERENCES

1. Lock, R. C. "A Review of Methods for Predicting Viscous Effects on Aerofoils and Wings at Transonic Speeds." AGARD-CPP-291, 1980.

2. Melnik, R. E. "Turbulent Interactions on Airfoils at Transonic Speeds — Recent Developments." AGARD-CPP-291, 1980.

3. Le Balleur, J. C. "Viscous-Inviscid Coupling Calculations for Two and Three Dimensional Flows." von Karman Institute for Fluid Dynamics, Lecture Series 1982-04, March 29-April 2, 1982.

4. Whitfield, D. L., Swafford, T. W. and Jacocks, J. L. "Calculation of Turbulent Boundary Layers with Separation and Viscous-Inviscid Interaction." *AIAA Journal*, Vol. 19, No. 10, October 1981, pp. 1315-1322.

5. Whitfield, D. L. "Integral Solution of Compressible Turbulent Boundary Layers Using Improved Velocity Profiles." AEDC-TR-78-42 (AD-A062946), December 1978.

6. Jameson, A., Schmidt, W., and Turkel, E. "Numerical Solutions of the Euler Equations by Finite Volume Methods Using Runge-Kutta Time-Stepping Schemes." AIAA Paper No. 81-1259, presented at AIAA Fourteenth Fluid and Plasma Dynamics Conference, Palo Alto, California, June 23-25, 1981.

7. Liepmann, H. W. and Roshko, A. *Elements of Gasdynamics.* John Wiley and Sons, Inc., New York, 1957.

8. Winter, F. G. and Gaudet, L. "Turbulent Boundary Layer Studies at High Reynolds Numbers at High Mach Numbers Between 0.2 and 2.8." Aeronautical Research Council R&M No. 3712, London, December 1970.

9. White, F. M. *Viscous Fluid Flow.* McGraw-Hill Book Co., Inc., New York, 1974.

10. Cebeci, T. and Smith, A. M. O. *Analysis of Turbulent Boundary Layers.* Academic Press, Inc., New York, 1974.

11. Whitfield, D. L., Swafford, T. W. and Donegan, T. L. "An Inverse Integral Computational Method for Compressible Turbulent Boundary Layers." *Transport Phenomena in Fluid Mechanics.* Springer-Verlag, Berlin, 1982, pp. 294-302.

12. Nash, J. F. "A Practical Calculation Method for Compressible Turbulent Boundary Layers in Two-Dimensional and Axisymmetric Flow." Lockheed-Georgia Company Research Memorandum ER-9428, Marietta, Georgia, August 1967.

13. Goldstein, S. "On Laminar Boundary-Layer Flow Near a Position of Separation." *Quarterly Journal of Mechanics and Applied Mathematics*, Vol. 1 (Part 1) 1948, pp. 43-69.

14. Swafford, T. W. "Analytical Approximation of Two-Dimensional Separated Turbulent Boundary-Layer Velocity Profiles." AEDC-TR-79-99 (AD-A091204), October 1980.

15. Catherall, D. and Mangler, K. W. "The Integration of the Two-Dimensional Laminar Boundary-Layer Equations Past the Point of Vanishing Skin Friction." *Journal of Fluid Mechanics*, Vol. 26 (Part 1), September 1966, pp. 163-182.

16. Cousteix, J., LeBalleur, J. C. and Houdeville, R. "Calculation of Unsteady Turbulent Boundary Layers in Direct or Inverse Mode, Including Reverse Flows-Analysis of Singularities." La Recherche Aerospatiale Report No. 1980-3 (English translation), Chatillon, France, May-June 1980.

17. Cook, P. H., McDonald, M. A. and Firmin, M. C. P. "Aerofoil RAE 2822-Pressure Distribution, and Boundary Layer and Wake Measurements." AGARD WG 04, United Kingdom, July 1977.

18. Simpson, R. L. Strickland, J. H. and Barr, P. W. "Features of a Separating Turbulent Boundary Layer in the Vicinity of Separation." *Journal of Fluid Mechanics*, Vol. 79, March 1977, pp. 553-594.

19. Simpson. R. L., Chew, Y.-T., and Shiraprasad, B. G. "The Structure of a Separating Turbulent Bounday Layer. Part 1. Mean Flow and Reynolds Stresses." *Journal of Fluid Mechanics*, Vol. 113, December 1981, pp. 23-51.

20. Lighthill, M. J. "On Displacement Thickness." *Journal of Fluid Mechanics*, Vol. 4 (Part 4), August 1958, pp. 383-392.

21. Carter, J. E. "A New Boundary-Layer Inviscid Iteration Technique for Separated Flow." AIAA Paper No. 79-1450, presented at AIAA Twelfth Fluid and Plasma Dynamics Conference, Williamsburg, Virginia, July 23-25, 1979.

APPENDIX A
DERIVATION OF EQUATIONS SOLVED BY UNSTEADY DIRECT METHOD

All flow parameters are evaluated at the boundary-layer edge. The subscript "e" has been eliminated and is understood.

Expanding Eq. (17) and multiplying by u will yield

$$\frac{\partial \delta^*}{\partial t} - \frac{\partial \theta_\varrho}{\partial t} = \frac{uc_f}{2} - \frac{1}{\varrho u} \frac{\partial}{\partial x}(\varrho u^2 \theta) - \delta^* \frac{\partial u}{\partial x} - \frac{\delta^*}{\varrho u} \frac{\partial}{\partial t}(\varrho u) + \frac{\theta_\varrho}{\varrho} \frac{\partial \varrho}{\partial t}$$

$$= b_1(c_f, \theta, \delta^*, \theta_\varrho) \qquad (A\text{-}1)$$

Expanding Eq. (21) and multiplying by 2u will yield

$$\frac{\partial \theta}{\partial t} + \frac{\partial \delta^*}{\partial t} - \frac{\partial \theta_\varrho}{\partial t} = 2u \frac{c_f D_E}{2} - \frac{1}{\varrho u^2} \frac{\partial}{\partial x}(\varrho u^3 \theta^*) - 2(\delta^* - \delta_u^*) \frac{\partial u}{\partial x}$$

$$- \frac{2(\theta_\varrho - \delta_u^*)}{u} \frac{\partial u}{\partial t} - \frac{1}{\varrho u^2} \left[\theta \frac{\partial}{\partial t}(\varrho u^2) + \delta^* \frac{\partial}{\partial t}(\varrho u^2) - \theta_\varrho \frac{\partial}{\partial t}(\varrho u^2)\right]$$

$$= b_2(c_f, D_E, \theta^*, \delta^*, \delta_u^*, \theta_\varrho, \theta) \qquad (A\text{-}2)$$

$$\frac{\partial \theta}{\partial t} = b_2 - b_1 \qquad (A\text{-}3)$$

Using the definitions $\delta^* = H_\delta \cdot \theta^*$ and $\theta_\varrho = H_{\theta_\varrho} \theta$, expanding Eq. (A-1) and collecting terms gives

$$\left(H_{\delta^*} - H_{\theta_\varrho}\right) \frac{\partial \theta}{\partial t} - \theta \left(\frac{\partial}{\partial t} H_{\theta_\varrho} - \frac{\partial H_{\delta^*}}{\partial t}\right) = b_1 \qquad (A\text{-}4)$$

But, H and H_{θ_ϱ} are functions of $\overline{H}$ and M_e from Whitfield's correlations. Using the chain rule and assuming $\partial M_e / \partial t = 0$ gives the final form for Eq. (A-4):

$$\left(H_{\delta^*} - H_{\theta_\varrho}\right) \frac{\partial \theta}{\partial t} - \theta \left(\frac{\partial}{\partial H} H_{\theta_\varrho} - \frac{\partial H_{\delta^*}}{\partial H}\right) \frac{\partial H}{\partial t} = b_1 \qquad (A\text{-}5)$$

For the final equations, solve for $\partial\theta/\partial t$ and $\partial\overline{H}/\partial t$ between Eqs. (A-3) and (A-5) to give

$$\frac{\partial\theta}{\partial t} = b_2 - b_1 \tag{A-6}$$

$$\frac{\partial\overline{H}}{\partial t} = \frac{b_1 - (H_{\delta^*} - H_{\theta_Q}]\dfrac{\partial\theta}{\partial t}}{\theta\left(\dfrac{\partial}{\partial\overline{H}}H_{\theta_Q} - \dfrac{\partial H_{\delta^*}}{\partial\overline{H}}\right)} \tag{A-7}$$

APPENDIX B
DERIVATION OF EQUATIONS SOLVED BY UNSTEADY INVERSE METHOD

In a similar fashion as in Appendix A, expanding Eq. (17) and multiplying by u/θ results in

$$\frac{H_{\delta^*}}{u}\frac{\partial u}{\partial t} = -\frac{u}{\theta}\frac{\partial \theta}{\partial x} - (2 + H_{\delta^*})\frac{\partial u}{\partial x} + \frac{c_f}{2}\frac{u}{\theta} + \frac{1}{\theta}\frac{\partial}{\partial t}(\theta_\varrho - \delta^*)$$

$$-\frac{u}{\varrho}\frac{\partial \varrho}{\partial x} - \frac{H_{\delta^*} - H_{\theta_\varrho}}{\varrho}\frac{\partial \varrho}{\partial t} = c_2 \tag{B-1}$$

Expanding Eq. (21) and multiplying by $2u/\theta$ results in

$$\frac{1}{\theta}\frac{\partial \theta}{\partial t} + \frac{1}{u}\left[2\left(1 + H_{\delta^*} - \frac{\delta_u^*}{\theta}\right)\right]\frac{\partial u}{\partial t} = -\frac{u}{\theta}H_{\delta^*}\frac{\partial \theta}{\partial x}$$

$$-\left[3H_{\theta^*} + 2\left(H_{\delta^*} - \frac{\delta_u^*}{\theta}\right)\right]\frac{\partial u}{\partial x} + \frac{c_f D_E u}{\theta} - u\frac{\partial H_{\theta^*}}{\partial x} \tag{B-2}$$

$$-\frac{1}{\theta}\frac{\partial}{\partial t}(\delta^* - \theta_\varrho) - \frac{uH_{\theta^*}}{\varrho}\frac{\partial \varrho}{\partial x} - \frac{(1 + H_{\delta^*} - H_{\theta_\varrho})}{\varrho}\frac{\partial \varrho}{\partial t} = c_1$$

This pair of equations may now be solved for $\partial\theta/\partial t$ and $\partial u/\partial t$ by Cramer's rule:

Defining

$$A_{11} = \frac{1}{\theta},$$

$$A_{12} = \frac{1}{u}\left[2\left(1 + H_{\delta^*} - \frac{\delta_u^*}{\theta}\right)\right],$$

$$A_{21} = 0,$$

$$A_{22} = \frac{H_{\delta^*}}{u};$$

49

then

$$\frac{\partial \theta}{\partial t} = \frac{A_{22}\, c_1 - A_{12}\, c_2}{A_{11}\, A_{22} - A_{12}\, A_{21}} = \frac{A_{22}\, c_1 - A_{12}\, c_2}{A_{11}\, A_{22}} \qquad \text{(B-3)}$$

$$\frac{\partial u}{\partial t} = \frac{A_{11}\, c_2 - A_{21}\, c_1}{A_{11}\, A_{22} - A_{12}\, A_{21}} = \frac{c_2}{A_{22}} \qquad \text{(B-4)}$$

These equations can be solved as long as the denominator ($H_{\delta^*}/u\theta$) does not approach zero (i.e., where $H_{\delta^*} \to 0$ or $u\theta \to \infty$). This condition will not apply since $H_{\delta^*} \neq 0$ and $u\theta$ is finite.

Both b_1 and b_2 in the direct method, and c_1 and c_2 in the inverse method include derivatives in time of flow parameters other than the ones sought in the solution process. It should be noted that the time-dependent terms are set to zero in the formulation to solve the equations. The end result is to obtain a steady-state solution in which these terms have no influence. However, during the solution process, an assumption must be made for these terms.

NOMENCLATURE

$A_{11}, A_{12},$ A_{21}, A_{22}	Denotes elements of the solution matrix (Appendix B)
b_1, b_2	Functions defined in Appendix A
C_p	Pressure coefficient, $(p-p_\infty)/(1/2\ q_\infty^2)$
c	Airfoil chord
c_1, c_2	Functions defined in Appendix B
c_f	Local skin friction coefficient, $2\tau_0/(\varrho_e u_e^2)$
D_E	Shear work integral term, defined by Eq. (20)
e	Energy, defined by Eq. (5)
F_{ij}	Parameter used in Navier-Stokes equations, defined by Eq. (3)
f_{ij}	Parameter used in Navier-Stokes equations, defined by Eq. (3)
G	Parameter used in Navier-Stokes equations, defined by Eq. (2)
H	Incompressible shape factor, δ^*/θ
H_{δ^*}	Shape factor based on δ^*, defined by Eq. (24)
$H_{\delta^*_u}$	Shape factor based on δ^*_u, defined by Eq. (26)
H_{θ^*}	Shape factor based on θ^*, defined by Eq. (25)
H_{θ_ϱ}	Shape factor based on θ_ϱ, defined by $H_{\theta_\varrho} = \theta_\varrho/\theta$
M	Mach number
p	Static pressure
q_i	The heat flux component

51

q_∞	Free-stream dynamic pressure, $\varrho_\infty u_\infty^2/2$
Re/c	Reynolds number based upon airfoil chord length, $\varrho_\infty u_\infty c/\mu_\infty$
Re_θ	Reynolds number based upon the momentum thickness, $\varrho_e u_e \theta/\mu_e$
t	Time
u	Velocity in the x-direction
v	Velocity in the y-direction
x	Coordinate along body surface
x_1, x_2, x_3	Arbitrary orthogonal coordinate system
y	Coordinate normal to the body surface

Greek Symbols

α	Angle of attack
γ	Ratio of specific heats
δ_{ij}	Kronecker delta
δ^*	Boundary-layer displacement thickness, defined by Eq. (13)
δ_u^*	Boundary-layer velocity thickness, defined by Eq. (18)
η	Bulk viscosity
θ	Boundary-layer momentum thickness, defined by Eq. (14)
θ^*	Boundary-layer energy thickness, defined by Eq. (19)
θ_ϱ	Boundary-layer density thickness, defined by Eq. (15)
λ	Second coefficient of viscosity

μ	Molecular or first coefficient of viscosity
ν	Kinematic viscosity coefficient
ϱ	Density
$-<\varrho u'v'>$	Reynolds stress
$(\varrho v)_n$	Local normal mass flux, defined by Eq. (30)
σ_{ij}	Deviatoric stress tensor
τ	Total shear stress
τ_{ij}	Denotes the viscous stress tensor
ω	Relaxation parameter in Eq. (31)

Subscripts

e	Boundary-layer edge conditions
o	Wall conditions
∞	Free-stream conditions

Superscripts

$(-)$	Low speed or incompressible value